

Effect of Rheology and Slip on Lubricant Deformation and Disk-to-Head Transfer during Heat-Assisted Magnetic Recording (HAMR)

Siddhesh V. Sakhalkar · David B. Bogy

Received: date / Accepted: date

Abstract The high temperature laser heating during Heat-Assisted Magnetic Recording (HAMR) causes the media lubricant to deform and transfer to the head via evaporation/condensation. The ability of the lubricant to withstand this writing process and sufficiently recover post-writing is critical for robust read/write performance. Moreover, the media-to-head lubricant transfer causes a continuous deposition of contaminants originating from the media at the head Near Field Transducer, challenging the reliability of HAMR drives. Most previous studies on the effects of laser exposure on lubricant depletion have assumed the lubricant to be a viscous fluid and have modeled its behavior using traditional lubrication theory. However, Perfluoropolyether lubricants are viscoelastic fluids and are expected to exhibit a combination of viscous and elastic behavior at the timescale of HAMR. In this paper, we introduce a modification to the traditional Reynolds lubrication equation using the Linear Maxwell constitutive equation and a slip boundary condition. We study the deformation and recovery of the lubricant due to laser heating under the influence of thermo-capillary stress and disjoining pressure. Subsequently, we use this modified lubrication equation to develop a model that predicts the media-to-head lubricant transfer during HAMR. This model simultaneously determines the deformation and evaporation of the viscoelastic lubricant film on the disk, the diffusion of the vapor phase lubricant in the air bearing and the evolution of the condensed lubricant film on the head. We investigate the effect of viscoelasticity, lubri-

cant type (Zdol vs Ztetraol), molecular weight, slip and disjoining pressure on the lubricant transfer process.

Keywords Hard Disk Drives · Heat-Assisted Magnetic Recording · Lubricant · Viscoelasticity · Rheology · Slip · Contamination · Smear

1 Introduction

Heat-Assisted Magnetic Recording (HAMR) is one of the leading technologies that is essential to achieve storage densities beyond 1 Tb/in² in hard disk drives. However, reliability of the head-disk interface (HDI) during high temperature transient laser heating still remains a major challenge that needs to be addressed before HAMR can be made into a robust commercial product [1].

One critical component of the HDI is the lubricant coating on the disk (typically from the Perfluoropolyether (PFPE) family) that protects the disk and the head from damage during intermittent contacts. During HAMR, a complex laser delivery system exposes the magnetic media to a high temperature in order to reduce its coercivity during writing. The high temperature gradient on the media causes the lubricant to deform and deplete under the influence of driving forces such as thermo-capillary stress, evaporation and degradation. The lubricant must be able to withstand this writing process and sufficiently recover the depletion and accumulation zones so as to allow for stable flying heights and reliable read/write performance.

Numerous works in the literature have investigated lubricant behavior during HAMR using continuum models, while assuming the lubricant to be a purely viscous material [2–5]. However, experiments show that PFPE lubricants are viscoelastic fluids [6–8] and can behave like viscous fluids or elastic solids or a combination of

S. V. Sakhalkar (✉) · D. B. Bogy
Computer Mechanics Laboratory, Department of Mechanical Engineering, University of California at Berkeley, Berkeley, CA 94720, USA
Tel.: +1-650-4574999
E-mail: siddhesh_sakhalkar@berkeley.edu

both depending on the flow timescale [9]. Sarabi & Bogy studied the effect of viscoelasticity on lubricant behavior during HAMR using a Finite Element implementation of the Linear Maxwell model in ANSYS [10]. They found that the lubricant exhibits elastic behavior with instantaneous deformations. However, this model solves the complete 3D equations of motion, failing to take advantage of the lubrication approximation. Moreover, disjoining pressure was linearized to ease computation speed and the effect of evaporation was not included. In this study, we introduce a modified Reynolds lubrication equation (2D) for the viscoelastic fluid using the Linear Maxwell model and demonstrate similar results to the 3D ANSYS model. Our model uses non-linear disjoining pressure and includes evaporation. Experiments by Mate et al. on lubricant migration on the slider suggest that slippage might be a dominant mechanism when the lubricant is subjected to high shear stresses [11]. Accordingly, we also investigate the effect of inclusion of a slip boundary condition on lubricant behavior under high thermo-capillary stress during HAMR.

Another major tribological challenge in HAMR is the formation of write-induced head contamination at the near field transducer (NFT) [12–17]. Kiely et al. [12] reported measurements of contamination thickness as a function of write time for a variety of different heads in different operating conditions. They observed that the contamination begins soon after the laser is turned on (< 1 s) and grows until the contamination height reaches the head-disk clearance. Once the head contamination contacts the media surface, the disk motion generates a smear down-track of the NFT. Xiong et al. [13] also reported deposition of materials on the head after HAMR writing. One possible mechanism that has been proposed for this contamination is lubricant desorption from the disk and adsorption on the head through thermodynamic driving forces [12]. During HAMR, the media is locally heated to its Curie temperature (~ 500 °C), causing the disk lubricant to evaporate and form vapor in the air bearing. The peak temperature of the head is lower than that of the disk (~ 300 °C). This temperature difference causes the lubricant to evaporate from the disk and condense on the relatively cooler head. The lubricant acts as a carrier, causing a continuous deposition of media contaminants at the NFT. Tani et al. used a pin-on-disk test to demonstrate smear growth on the pin surface when lubricated disk with adsorbed contaminant, siloxane was exposed to laser heating [17].

Understanding the mechanism of media-to-head lubricant and contaminant transfer is crucial in order to eliminate or control its effect and develop reliable HAMR drives. Lubricant transfer at the head-disk interface has been studied using molecular dynamics (MD) [18–21].

Dai et al. predicted the formation of a lubricant bridge between the disk and the slider due to HAMR heating using MD simulations [18]. Marchon & Saito [4] presented fluid dynamics simulation results of unfunctionalized lubricant Z on the disk under HAMR laser heating that agreed well with much more computationally expensive MD simulations. Moreover, experiments on unfunctionalized and functionalized lubricant behavior under air shear by Mate et al. and Scarpulla et al. [22, 23] show that flow of molecularly thin films can still be described by continuum theory with the adoption of an effective viscosity. Continuum mechanics offers a cost-effective yet accurate method to study lubricant behavior with realistic domain sizes and simulation times.

In our previous study [24], we developed a viscous continuum model that predicts the media-to-head lubricant transfer during HAMR for Zdol. This model determines the thermo-capillary stress driven deformation and evaporation of the lubricant film on the disk, the convection/diffusion of the lube vapor in the air bearing and the evolution of the condensed lubricant on the head. We found that several angstroms of lubricant transfer occurs after 2 ns of laser heating. Starting with a 1.2 nm film on the disk, the disk and head lube thicknesses after 2 ns at the NFT were 0.59 nm & 0.83 nm, respectively. The equilibrium vapor pressure of Zdol at 0.59 nm & 500 °C (disk conditions) is 0.3 MPa and at 0.83 nm & 310 °C (head conditions) is 5×10^{-4} MPa [24]. The partial pressure of the lube vapor at the NFT at 405 °C was 0.07 MPa. Thus, the partial pressure of the lube vapor in the air bearing is smaller than equilibrium vapor pressure of the disk lubricant, but larger than the equilibrium vapor pressure of the head lubricant. This drives the evaporation of lubricant from the disk and subsequent condensation on the head. However, this model assumes a viscous constitutive law for the lubricant, which in reality is a viscoelastic fluid. In this study, we improve this model to include the effect of viscoelasticity and slip on lubricant transfer. We study the effect of lubricant type (Zdol vs Ztetraol), molecular weight and disjoining pressure on the transfer process.

2 Rheology

2.1 Linear Viscoelasticity and Deborah Number

Under small deformation gradients, viscoelastic fluids exhibit linear behavior. The most basic model for a linear viscoelastic fluid is the Linear Maxwell model (single

stage), which is described by the following equation:

$$\begin{aligned} \boldsymbol{\sigma} &= -p\mathbf{I} + \boldsymbol{\tau} \\ \frac{\boldsymbol{\tau}}{\eta} + \frac{1}{G} \frac{\partial \boldsymbol{\tau}}{\partial t} &= \nabla \mathbf{v} + (\nabla \mathbf{v})^T \end{aligned} \quad (1)$$

Here $\boldsymbol{\sigma}$ is the Cauchy stress, p is the pressure of the incompressible fluid, $\boldsymbol{\tau}$ is the extra stress and \mathbf{v} is the velocity. Viscosity η and shear modulus G are related to Maxwell relaxation time λ by $\eta = G\lambda$.

A viscoelastic fluid can exhibit viscous or elastic behavior depending on the flow timescale. In order to characterize this behavior, the non-dimensional parameter "Deborah number" is introduced by normalizing the maxwell relaxation time by the flow timescale: $De = \frac{\lambda}{t_s}$. When $De \ll 1$, the material behaves like a viscous fluid, when $De \gg 1$ it behaves like an elastic solid and for $De \sim 1$ the material has both viscous and elastic characteristics. For the lubricant under HAMR, the flow time scale may be defined as $t_s = \frac{L}{U}$, where L is the laser FWHM (set as 20 nm in this study) and U is the disk velocity (~ 10 m/s), thus $De = \frac{\lambda U}{L}$ [10].

2.2 Bulk Lubricant Rheology

Bulk rheological properties of PFPE lubricants have been studied by measuring their viscosity (η), storage modulus (G'), loss modulus (G'') via steady-shear and dynamic oscillation measurements using rotational rheometers [6–8]. Kono et al. investigated the rheological properties of PFPEs with different molecular weights and end-groups [6]. Karis measured the dynamic moduli of several PFPEs including Zdol 2500 and Ztetraol 2000 between 1 and 100 rad/s at temperatures from -20 to 100 °C [8]. The PFPEs were found to be linear viscoelastic at these conditions (dynamic strain amplitude of 5%). The data measured at low temperatures was transformed to high frequency through time-temperature superposition with Williams Landel Ferry (WLF) Coefficients:

$$\log(a_{T_0}) = \frac{-C_1(T - T_0)}{C_2 + (T - T_0)} \quad (2)$$

Here reference temperature T_0 is the glass transition temperature of the PFPE and C_1 and C_2 are WLF coefficients with respect to T_0 . Upto 3 linear Maxwell elements (i.e. 3 sets of shear moduli G_i and Maxwell relaxation times τ_i) were derived for each PFPE from the data for G' , G'' versus ωa_{T_0} . The measurements for τ_i and G_i show that for these multistage models, one of the stages is dominant ($\tau_1 \gg \tau_2, \tau_3$). To simplify calculations, we consider only the dominant stage and reduce Karis' model to a single-stage one (i.e. Linear

Maxwell model - Eq. (1)) with shear modulus G_{bulk} ($= G_1$) and viscosity η_{bulk} . Accordingly the viscosity as a function of temperature is given by:

$$\eta_{bulk}(T) = \eta_{bulk}(T_0)a_{T_0}(T) \quad (3)$$

where $\eta_{bulk}(T_0)$ is the viscosity at the reference temperature T_0 and $a_{T_0}(T)$ is given by Eq. (2). The Maxwell relaxation time can be obtained as: $\lambda_{bulk} = \frac{\eta_{bulk}}{G_{bulk}}$. The Maxwell relaxation time and viscosity have the same temperature shift function and thus the shear modulus is independent of temperature. T_0 , C_1 , C_2 , $\eta_{bulk}(T_0)$, G_{bulk} for Zdol 2500 and Ztetraol 2000 are tabulated in Table 1. Viscosity of Ztetraol as a function of temperature using Eqs. (2), (3) is plotted in Fig. 1.

Lubricant	Zdol 2500	Ztetraol 2000
T_0	-113.6 °C	-112.2 °C
C_1	13.62	23.22
C_2	59.72	45.81
$\eta_{bulk}(T_0)$	4.16 e+8 Pa-s	2.34 e+17 Pa-s
G_{bulk}	51.9 kPa	36.6 kPa

Table 1: Glass transition temperature T_0 , WLF coefficients C_1 , C_2 , viscosity η_{bulk} at T_0 and shear modulus G_{bulk} for Zdol 2500 and Ztetraol 2000 [8]

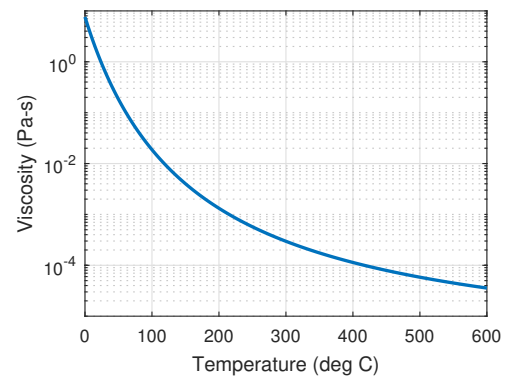


Fig. 1: Bulk Ztetraol viscosity (Pa-s) versus temperature (°C) using oscillatory measurements and time-temperature superposition (Eqs. (2), (3)) [8]

2.3 Thin Film Lubricant Rheology

Ruths & Granick measured the dynamic moduli G' , G'' of thin unfunctionalized and functionalized PFPE films (2.8 nm Z03, 3.3 nm Zdol 2100, 6.6 nm Zdol 4000) at normal pressures of 1 and 3 MPa and shear rates

of 10^{-2} to 10^5 s^{-1} [25]. The properties were measured by shearing the films between two mica surfaces using a surface force apparatus (SFA). They found that the unfunctionalized Z03 displayed elastic behavior in the entire frequency range of 1.3-130 Hz with large, frequency independent moduli (in the regime of linear response i.e. small-amplitude oscillatory shear). Zdol 2100 also exhibited elastic behavior with frequency independent moduli ($G' \sim 1$ MPa, G'' was one order of magnitude smaller) at higher normal pressure of 3 MPa. Under large deformations, the moduli dropped significantly due to shear thinning/slip. These results suggest that the Maxwell relaxation time and zero-shear viscosity of nano-scale films are several orders of magnitude higher than the bulk values. More recently Itoh et al. measured the dynamic moduli of Z03 and Zdol at higher frequencies using a Fiber Wobbling Method (FWM) [26, 27]. They found that as the film thickness decreases, both the viscosity and elasticity of the lubricant increase.

Mate & Marchon studied the shear response of similar unfunctionalized PFPE films when subjected to air shear stress of 20 - 200 Pa (comparable shear rates to SFA) using a blow-off technique [22]. They found that molecularly thin films partially confined by a single solid surface do not solidify (unlike SFA results) and display viscous behavior. They attributed the "solid like behavior" in the SFA experiment to confinement of molecules between two solid surfaces with applied pressure. Scarpulla et al. [23] studied the shear properties of molecularly thin films of the functionalized lubricant Zdol using blow-off and found that its flow can be described by an enhanced effective viscosity (larger than the bulk viscosity for functionalized lubricants). Karis et al. studied lubricant spin-off from magnetic disks and reported that the effective viscosity of Zdol increases exponentially with decrease in thickness [28].

More recently Marchon et al. [29] and Mate et al. [11] studied the migration of the functionalized lubricant Ztetraol on the head under higher air shear stresses (~ 500 kPa in [29], ~ 10 kPa in [11]). They found that the effective thin-film viscosity is either similar to or smaller than the bulk viscosity (in contrast with previous studies [23, 28] where the effective viscosity was larger than the bulk viscosity). Moreover, the effective viscosity was found to decrease with decreasing lubricant thickness. This apparent discrepancy was attributed to slip caused by high shear stresses. As the film thickness is reduced, slip becomes a more dominant migration mechanism, which would manifest itself within the viscous flow simulation as a lower viscosity.

Experiments on lubricant films on a solid substrate under air shear demonstrate that the behavior of thin films confined by a single solid and confined between

two solids are significantly different. Dynamic properties from SFA/FWM experiments cannot be directly used to study the behavior of lubricant under HAMR laser heating (confined by a single solid - the disk). Hence we use the bulk rheological properties from Table 1 with appropriate thin-film enhancement factors. Karis et al. [28] found a viscosity enhancement factor of ~ 13 for 1 nm thick Zdol 4000. Accordingly, we assume that the effective viscosity for both Zdol and Ztetraol is 13 times the bulk viscosity determined using Eq. (3) (i.e. $\eta_{eff} = 13 \times \eta_{bulk}$). To account for slippage caused by high shear stresses, we apply the Navier slip boundary condition, which assumes that the slip velocity \mathbf{v}_{slip} is directly proportional to the wall shear stress $\boldsymbol{\tau}_{wall}$:

$$\mathbf{v}_{slip} = \frac{b}{\eta} \boldsymbol{\tau}_{wall} \quad (4)$$

Here b is the slip length. Other non-linear slip boundary conditions are also available such as power-law dependence on wall shear stress or a threshold-type slip [30]. However, the Navier slip boundary condition is the simplest one and is commonly used to study the combined effect of slip and viscoelasticity on thin polymer film evolution [31, 32]. Since no quantitative data is available in literature about the effect of confinement (by a single solid) on the Maxwell relaxation time, we assume that $G_{eff} = 13 \times G_{bulk}$ and $\lambda_{eff} = \lambda_{bulk}$ in the baseline simulation (so that $\eta_{eff} = G_{eff} \lambda_{eff}$). We also perform a sensitivity analysis to see how the lubricant behavior changes if the enhancement factor of 13 is partially absorbed by λ_{eff} and G_{eff} (Refer Section 3.3.5).

3 Effect of Viscoelasticity on Disk Lubricant Deformation during HAMR

3.1 Lubrication Theory based on Linear Maxwell Model

3.1.1 Lubrication Equation Derivation

We consider the generic problem of a thin lubricant film of thickness $h(x, y, t)$ on a flat substrate, moving at a constant linear speed U . The frame of reference is moving along with the substrate (so that the substrate appears to be rest). The co-ordinate system is defined such that the z axis is along the lubricant thickness and the x axis is along the direction of the substrate velocity. The top surface of the lubricant ($z = h$) is free to evolve under the influence of external shear stress $\boldsymbol{\tau}_b(x, y, t) = \tau_{b,x} \mathbf{e}_x + \tau_{b,y} \mathbf{e}_y$ and external pressure $p_b(x, y, t)$. We assume that the characteristic dimension in the z direction, h_0 is much smaller than the characteristic dimension in the x and y directions, L . The

inertial terms in the equation of motion are assumed to be small compared to the extra stress terms. We also assume that the stresses τ_{xx} , τ_{xy} , τ_{yy} , τ_{zz} are smaller than or comparable to τ_{xz} , τ_{yz} . With these assumptions, the Cauchy equation of motion, the constitutive law (Eq. (1)) and the continuity equation simplify to [9]:

$$\begin{aligned} -\frac{\partial p}{\partial x} + \frac{\partial \tau_{xz}}{\partial z} &= 0 \\ -\frac{\partial p}{\partial y} + \frac{\partial \tau_{yz}}{\partial z} &= 0 \\ \frac{\partial p}{\partial z} &= 0 \end{aligned} \quad (5)$$

$$\begin{aligned} \frac{\tau_{xz}}{\eta} + \frac{1}{G} \frac{\partial \tau_{xz}}{\partial t} &= \frac{\partial v_x}{\partial z} \\ \frac{\tau_{yz}}{\eta} + \frac{1}{G} \frac{\partial \tau_{yz}}{\partial t} &= \frac{\partial v_y}{\partial z} \end{aligned} \quad (6)$$

$$\begin{aligned} \frac{\partial h}{\partial t} + \frac{\partial q_x}{\partial x} + \frac{\partial q_y}{\partial y} + \frac{\dot{m}}{\rho} &= 0 \\ q_x &= \int_0^h v_x dz \\ q_y &= \int_0^h v_y dz \end{aligned} \quad (7)$$

Eq. (7) is obtained by integrating the continuity equation across the film thickness. Here ρ is the lubricant density and \dot{m} is the evaporation mass flux per unit time. v_x , v_y are the lubricant velocity components along x and y respectively and p is the lubricant pressure. Integrating Eq. (5) subject to boundary condition at $z = h$ ($\tau_{xz}|_{z=h} = \tau_{b,x}$, $\tau_{yz}|_{z=h} = \tau_{b,y}$, $p|_{z=h} = p(x, y, t) = p_b$), we obtain these shear stress profiles:

$$\begin{aligned} \tau_{xz} &= \frac{\partial p}{\partial x}(z - h) + \tau_{b,x} \\ \tau_{yz} &= \frac{\partial p}{\partial y}(z - h) + \tau_{b,y} \end{aligned} \quad (8)$$

We consider the linear Navier slip boundary condition (Eq. (4)) at $z = 0$ (with constant slip length b)

$$\begin{aligned} v_x|_{z=0} &= \frac{b}{\eta} \tau_{xz}|_{z=0} = \frac{b}{\eta} \left(-\frac{\partial p}{\partial x} h + \tau_{b,x} \right) \\ v_y|_{z=0} &= \frac{b}{\eta} \tau_{yz}|_{z=0} = \frac{b}{\eta} \left(-\frac{\partial p}{\partial y} h + \tau_{b,y} \right) \end{aligned} \quad (9)$$

Inserting the shear stress profiles from Eq. (8) into Eq. (6) and integrating using the boundary condition at

$z = 0$, we obtain the following velocity profiles:

$$\begin{aligned} v_x &= \frac{1}{\eta} \left[\frac{\partial p}{\partial x} \left(\frac{z^2}{2} - hz - bh \right) + \tau_{b,x} (z + b) \right] \\ &\quad + \frac{1}{G} \left[\frac{\partial^2 p}{\partial t \partial x} \left(\frac{z^2}{2} - hz \right) - \frac{\partial p}{\partial x} \frac{\partial h}{\partial t} z + \frac{\partial \tau_{b,x}}{\partial t} z \right] \\ v_y &= \frac{1}{\eta} \left[\frac{\partial p}{\partial y} \left(\frac{z^2}{2} - hz - bh \right) + \tau_{b,y} (z + b) \right] \\ &\quad + \frac{1}{G} \left[\frac{\partial^2 p}{\partial t \partial y} \left(\frac{z^2}{2} - hz \right) - \frac{\partial p}{\partial y} \frac{\partial h}{\partial t} z + \frac{\partial \tau_{b,y}}{\partial t} z \right] \end{aligned} \quad (10)$$

Inserting the velocity profiles from Eq. (10) into the integrated continuity Eq. (7), we arrive at the governing equation for the viscoelastic lubricant:

$$\begin{aligned} \frac{\partial h}{\partial t} + \frac{\partial}{\partial x} \left(-\frac{h^3}{3\eta} \frac{\partial p}{\partial x} + \frac{h^2}{2\eta} \tau_{b,x} - \frac{h^2 b}{\eta} \frac{\partial p}{\partial x} + \frac{hb}{\eta} \tau_{b,x} \right) \\ + \frac{\partial}{\partial x} \left(-\frac{h^3}{3G} \frac{\partial^2 p}{\partial t \partial x} - \frac{h^2}{2G} \frac{\partial p}{\partial x} \frac{\partial h}{\partial t} + \frac{h^2}{2G} \frac{\partial \tau_{b,x}}{\partial t} \right) \\ + \frac{\partial}{\partial y} \left(-\frac{h^3}{3\eta} \frac{\partial p}{\partial y} + \frac{h^2}{2\eta} \tau_{b,y} - \frac{h^2 b}{\eta} \frac{\partial p}{\partial y} + \frac{hb}{\eta} \tau_{b,y} \right) \\ + \frac{\partial}{\partial y} \left(-\frac{h^3}{3G} \frac{\partial^2 p}{\partial t \partial y} - \frac{h^2}{2G} \frac{\partial p}{\partial y} \frac{\partial h}{\partial t} + \frac{h^2}{2G} \frac{\partial \tau_{b,y}}{\partial t} \right) \\ + \frac{\dot{m}}{\rho} = 0 \end{aligned} \quad (11)$$

In this equation, $q_{viscous,x} = \left(-\frac{h^3}{3\eta} \frac{\partial p}{\partial x} + \frac{h^2}{2\eta} \tau_{b,x} \right)$ is the viscous volumetric flow rate per unit width (originating from the viscous part of the constitutive Eq. (6)), $q_{slip,x} = \left(-\frac{h^2 b}{\eta} \frac{\partial p}{\partial x} + \frac{hb}{\eta} \tau_{b,x} \right)$ is the volumetric flow rate per unit width due to slip (originating from the slip boundary condition: Eq. (9)) and $q_{elastic,x} = \left(-\frac{h^3}{3G} \frac{\partial^2 p}{\partial t \partial x} - \frac{h^2}{2G} \frac{\partial p}{\partial x} \frac{\partial h}{\partial t} + \frac{h^2}{2G} \frac{\partial \tau_{b,x}}{\partial t} \right)$ is the elastic volumetric flow rate per unit width (originating from the elastic part of the constitutive Eq. (6)). In the limit $De \ll 1$ and $b = 0$, i.e. $q_{elastic,x} = 0$ and $q_{slip,x} = 0$, this equation reduces to the classical Reynolds lubrication equation for viscous, incompressible fluids [3, 24].

3.1.2 Lubricant Driving Forces during HAMR Writing

The deformation of the lubricant under HAMR is driven by the thermo-capillary shear stress caused by the spatial temperature gradient. Assuming that surface tension γ decreases linearly with temperature, the external shear stress $\boldsymbol{\tau}_b = \tau_{b,x} \mathbf{e}_x + \tau_{b,y} \mathbf{e}_y$ in Eq. (11) for a quasi-parallel film ($|\nabla h| \ll 1$, $\mathbf{n} \approx \mathbf{e}_z$) is given by

$$\boldsymbol{\tau}_b = \frac{\partial \gamma}{\partial x} \mathbf{e}_x + \frac{\partial \gamma}{\partial y} \mathbf{e}_y = -c \left(\frac{\partial T}{\partial x} \mathbf{e}_x + \frac{\partial T}{\partial y} \mathbf{e}_y \right) \quad (12)$$

We assume $c \equiv -\frac{d\gamma}{dT} = 0.06 \text{ mN}/(m^\circ\text{C})$ [3]. The coordinate system is attached to the moving disk. In this frame, the disk appears to be stationary and the scanning thermal spot moves with speed U . Thus, the disk temperature profile is assumed to be a Gaussian curve with FWHM of 20 nm, moving with linear speed U . To keep the time derivatives finite, we apply the initial rise in temperature as a ramp of 2 ns.

Next, we consider contributions to external pressure p_b . Since lubricant pressure p is independent of z , $p = p_b$. The normal pressures applied to the film are the air bearing pressure, disjoining pressure and laplace pressure. Of these, the disjoining pressure has a dominant effect on lubricant diffusion. The timescale of lubricant deformation during HAMR is of the order of ns, while the effect of the air bearing pressure is expected to be on the order of seconds [33] and can be ignored. The laplace pressure can also be ignored unless the surface profile shows a sharp spatial variation. The van der Waals component of disjoining pressure is given by $\Pi_{vdw}(h) = \frac{A_{VLS}}{6\pi(h+d_0)^3}$ [34]. Here A_{VLS} is the Hamaker constant for the vapor-liquid-solid system. d_0 is a constant introduced to account for the finite size of the atoms and molecules within the lubricant film. We use the following values in this study: $A_{VLS} = 1 \times 10^{-19} \text{ J}$, $d_0 = 0.3 \text{ nm}$ [34]. For lubricants with reactive end-groups, the total disjoining pressure also has electrostatic and structural components [34]. However, for thin films ($\leq 1 \text{ nm}$, far from the typical dewetting thickness), the van der Waals component becomes dominant. Thus, p in Eq. (11) is given by

$$p = -\Pi(h) = -\frac{A_{VLS}}{6\pi(h+d_0)^3} \quad (13)$$

Finally, high temperatures during HAMR writing cause lubricant depletion due to evaporation and degradation. These effects are not considered in this section. The effect of evaporation will be discussed in Section 4.

Eq. (11) along with Eqs. (12), (13) describe the evolution of the lubricant height $h(x, y, t)$ under HAMR writing. We first discretize the time derivatives in Eq. (11) using the Implicit Euler method. The spatial derivatives are then discretized using the second order accurate finite difference schemes [35].

3.2 Non-linear Viscoelastic Effects

The Linear Maxwell model is not frame invariant and is valid only for small deformation gradients [36]. It is not clear if the linear model is a reasonable approximation to predict the lubricant deformation during HAMR. In order to convincingly answer this question, one would have to simulate the lubricant behavior us-

ing a non-linear viscoelastic constitutive equation (for example, differential model like the upper-convected Maxwell model [37] or integral model like the K-BKZ model) and compare the results with the linear model. When $De \gg 1$, Tanner suggests using a non-linear elastic model to predict the rapid deformation behavior of the viscoelastic material [9]. In fact, most non-linear viscoelastic models including the upper-convected Maxwell model and K-BKZ model reduce to some non-linear elastic model when $De \rightarrow \infty$. Hence, as a quick check, we compare the results of the Linear Maxwell model in the elastic limit (viscous terms suppressed), with the simplest non-linear elastic model - the incompressible neo-hookean model, which is described by the following equation:

$$\mathbf{P} = -p\mathbf{F}^{-T} + G\mathbf{F} \quad (14)$$

Here \mathbf{P} is the first Piola-Kirchhoff stress tensor and \mathbf{F} is the deformation gradient. G is the shear modulus and p is the pressure (Lagrange multiplier). Eq. (14) along with the Cauchy equation of motion (in referential form) and the incompressibility condition form the governing system of equations for the neo-hookean solid:

$$\begin{aligned} \rho_0 \mathbf{a} &= \text{Div} \mathbf{P} \\ \det \mathbf{F} &= 1 \end{aligned} \quad (15)$$

Here ρ_0 is the referential density, \mathbf{a} is the acceleration. Body forces are ignored. We simulate the behavior of the neo-hookean lubricant under HAMR using an ANSYS FEM model. We compare the results of this model with the prediction of the modified lubrication equation for the Linear Maxwell fluid, with viscous terms suppressed. The idea is to check if the prediction of the Linear Maxwell model (in elastic limit) is close to the neo-hookean result. If this is the case, it would be some justification for the assumption that the effect of the non-linear terms in the general viscoelastic case is small.

3.3 Results

3.3.1 Lubricant Deformation during HAMR: Viscous vs Viscoelastic Behavior

For the baseline simulation, we assume an initially uniform film of Ztetraol of thickness $h_0 = 1 \text{ nm}$ on the disk. The slip length b is set to 0. The lubricant is subjected to a moving laser spot of FWHM 20 nm at 10 m/s. At $t = 0$ the laser spot is centered at $x = 0, y = 0$, hence at $t = 20 \text{ ns}$, the laser spot is at $x = 200 \text{ nm}, y = 0$. The resultant temperature profile on the disk is a Gaussian with a peak of 500 °C. We plot the lubricant profile in

the down-track (x) direction (h vs x at $y = 0$) at 10 ns and 20 ns in Fig. 2. The lubricant profile is composed of a trough of depth 0.43 nm centered at the instantaneous laser position, with a trail of depth 0.1 nm. As the laser moves forward from $x = 100$ nm (at 10 ns) to $x = 200$ nm (at 20 ns), the trough follows the laser instantaneously, thus displaying an elastic behavior. The trail length keeps increasing as the laser moves forward, displaying a characteristic viscous behavior.

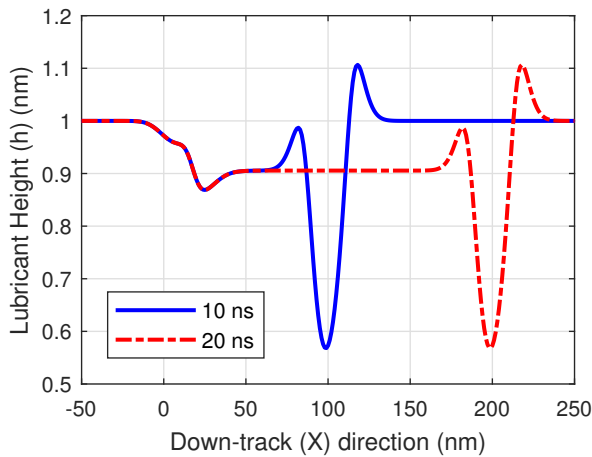
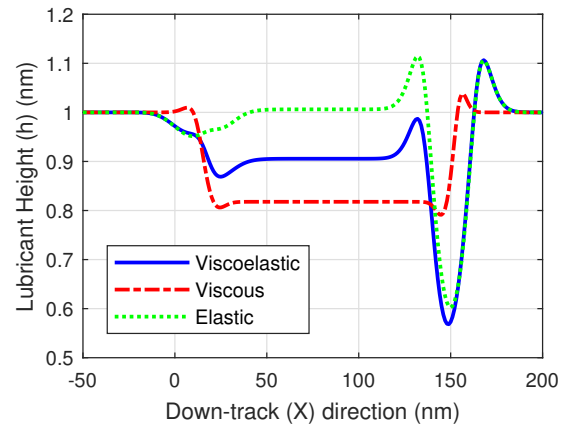
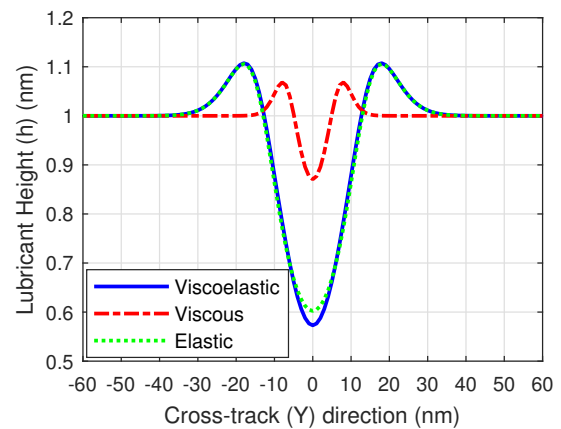


Fig. 2: Down-track lubricant (Ztetraol) profile (at $y = 0$) after 10 ns and 20 ns of laser irradiation. $T_{max} = 500$ °C, $U = 10$ m/s, FWHM = 20 nm, $b = 0$.

In order to distinguish between these two contrasting behaviors, we performed simulations for the viscous limit (elastic terms artificially suppressed: $q_{elastic} = 0$ in Eq. (11)) and elastic limit (viscous terms artificially suppressed: $q_{viscous} = 0$ in Eq. (11)). We plot the down-track (x) and cross-track (y) profiles of the viscoelastic, viscous and elastic solutions in Figs. 3a & 3b at the end of 15 ns of laser heating. The down-track profile (h vs x) is plotted at $y = 0$ and the cross-track profile (h vs y) is plotted at $x = 150$ nm (i.e. at the instantaneous position of the laser at $t = 15$ ns). The down-track profile shows that the purely elastic solution is composed of an instantaneously moving trough with no trail, whereas the purely viscous solution has no instantaneous trough (just a trail). The viscoelastic solution is a combination of both. The cross-track profile shows that the deformed lubricant width for the elastic/viscoelastic solution is much larger (almost twice) the width of the purely viscous solution. The purely elastic solution leaves behind a small residual trough of depth 0.05 nm between $x = -10$ nm and $x = 40$ nm. This trough was found to be a consequence of the initial temperature ramp from $t = 0$ to $t = 2$ ns. However, this trough does not affect the so-



(a) Down-track lubricant profile (at $y = 0$)



(b) Cross-track lubricant profile (at $x = 150$ nm)

Fig. 3: Lubricant profile (Ztetraol) after 15 ns of laser heating - viscous, elastic and viscoelastic profiles. $T_{max} = 500$ °C, $U = 10$ m/s, FWHM = 20 nm, $b = 0$.

lution at later times (the trough moves instantaneously with no trail apart from this initial residual trough) and thus can be ignored for the long term solution.

3.3.2 Comparison with Sarabi & Bogy

Sarabi & Bogy [10] used a Finite Element ANSYS model to describe the lubricant evolution during HAMR using the integral form of the Linear Maxwell model (Fig. 4). This model solves the complete 3D Cauchy equations of motion without the simplifications arising from the lubrication approximation. Here we compare the results of our modified lubrication equation (11) with the ANSYS model proposed in [10]. The ANSYS model uses a lagrangian description of the equations of motion with the initial undeformed lube as the referential configuration. Combining this approach with the lubrication approximation in Section 3.1.1, we arrive at the follow-

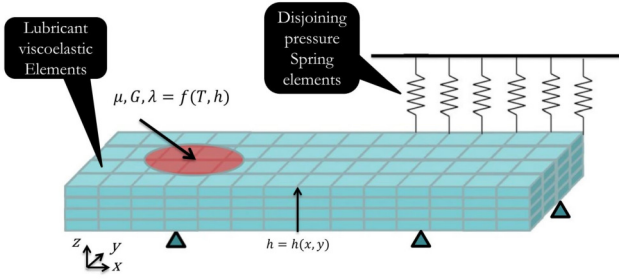


Fig. 4: 3D mesh used for FEA of the HAMR problem. Reprinted by permission from Springer Nature (Tribology Letters) [10], Copyright (2018).

ing Lagrangian description of lubricant height $h(X, t)$ (assuming no slip i.e. $b = 0$, no evaporation):

$$\begin{aligned} \frac{\partial h}{\partial t} + \frac{\partial}{\partial X} \left(-\frac{h_0^3}{3\eta} \frac{\partial p}{\partial X} + \frac{h_0^2}{2\eta} \tau_{b,x} \right) \\ + \frac{\partial}{\partial X} \left(-\frac{h_0^3}{3G} \frac{\partial^2 p}{\partial t \partial X} + \frac{h_0^2}{2G} \frac{\partial \tau_{b,x}}{\partial t} \right) \\ + \frac{\partial}{\partial Y} \left(-\frac{h_0^3}{3\eta} \frac{\partial p}{\partial Y} + \frac{h_0^2}{2\eta} \tau_{b,y} \right) \\ + \frac{\partial}{\partial Y} \left(-\frac{h_0^3}{3G} \frac{\partial^2 p}{\partial t \partial Y} + \frac{h_0^2}{2G} \frac{\partial \tau_{b,y}}{\partial t} \right) = 0 \end{aligned} \quad (16)$$

Here h_0 is the initial uniform (undeformed) lubricant height and X, Y are the spatial co-ordinates in the reference configuration (as opposed to x, y from Eq. (11) which are the spatial co-ordinates in the current configuration). We simulate the deformation of a 1 nm ($= h_0$) lube under a Gaussian temperature profile with a peak of 500 °C and FWHM of 20 nm, moving at a linear speed U of 10 m/s. Lubricant profiles in the down-track direction (at $y = 0$) at the end of 10 ns using Eq. (11), Eq. (16) and the ANSYS model from [10] are plotted in Fig. 5. The disjoining pressure (given by Eq. (13)) is modeled as a linear spring with constant stiffness per unit area of $1.95e+16$ N/m³ ($=$ value of $\frac{\partial p}{\partial h}$ at $h = 0.65$ nm) in all three models [10]. The ANSYS solution and the solution of Eq. (16) agree almost exactly, which confirms the validity of the lubrication approximation. The solution of Eq. (11) has a smaller width and depth than Eq. (16). This difference is attributed to the additional approximations involved in deriving Eq. (16) as opposed to Eq. (11). (Eq. (16) assumes that $\frac{\partial}{\partial X} \approx \frac{\partial}{\partial x}$).

3.3.3 Comparison between Linear Maxwell Model in Elastic Limit and Neo-hookean Model

In order to estimate the magnitude of non-linear viscoelastic effects, we study the lubricant deformation during HAMR using the neo-hookean model and compare

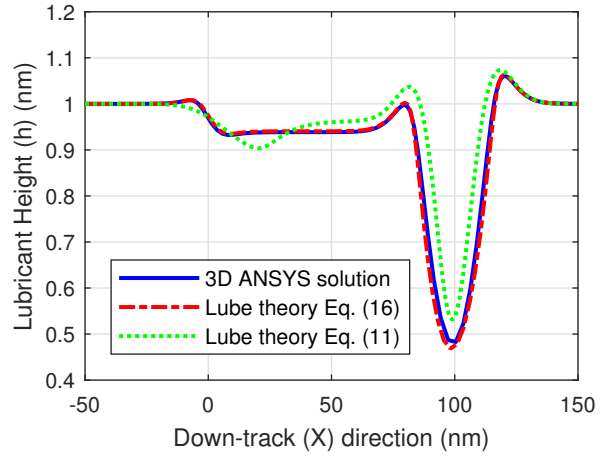


Fig. 5: Down-track lubricant (Ztetraol) profile (at $y = 0$) after 10 ns of laser irradiation - Comparison between 3D ANSYS solution [10] and lubrication theory solution using Eqs. (11) and (16). $T_{max} = 500$ °C, $U = 10$ m/s, FWHM = 20 nm, $b = 0$.

the results with the solution using the Linear Maxwell model, in the limit $De \rightarrow \infty$ (i.e. viscous terms artificially set to 0). To simplify the calculations, we consider a 2D form of the actual 3D problem (in the X-Z plane), where all quantities are assumed to be uniform in the Y direction. The effects of slip, evaporation and disjoining pressure are also ignored for simplicity. Accordingly, the governing equation for lubricant height $h(x, t)$ using the Linear Maxwell model is given by:

$$\frac{\partial h}{\partial t} + \frac{\partial}{\partial x} \left(\frac{h^2}{2G} \frac{\partial \tau_{b,x}}{\partial t} \right) = 0 \quad (17)$$

We simulate the deformation of a 1 nm lube for a peak disk temperature of 500 °C and laser FWHM of 20 nm. The laser speed U is kept high (30 m/s) so that the Deborah number is high and the error by setting the viscous terms to 0 is small. The lubricant profile in the down-track direction (x) at the end of 5 ns using Eq. (17) and the 2D neo-hookean ANSYS model is plotted in Fig. 6. We see that both solutions show the same behavior - an elastic trough centered at the instantaneous laser spot, with no trail. The only difference is that the Linear Maxwell solution leaves behind a small residual trough of depth ~ 0.1 nm between $x = -10$ nm and $x = 40$ nm, as explained in section 3.3.1. Both solutions have nearly the same trough width (~ 30 nm) and similar trough depths (min h is 0.77 nm for Linear Maxwell solution vs 0.74 nm for neo-hookean solution). The height of the side ridges is slightly larger for the neo-hookean model (max. h is 1.29 nm for Linear Maxwell solution vs 1.19 nm for

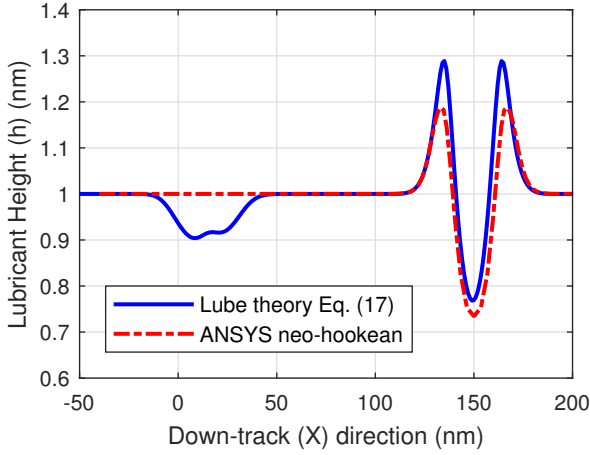
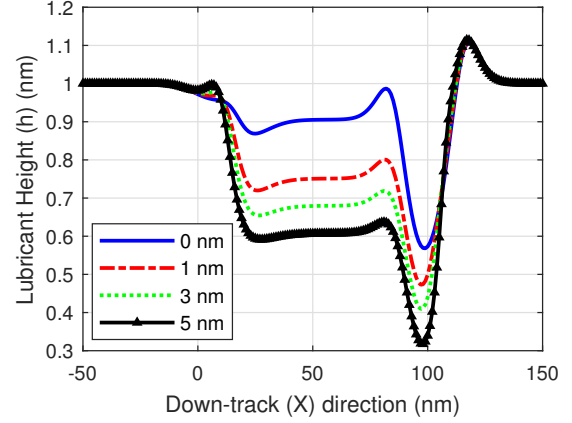


Fig. 6: Down-track lube profile (Ztetraol) after 5 ns of laser heating. Comparison between ANSYS neo-hookean solution and lubrication theory solution using Eq. (17). $T_{max} = 500$ °C, $U = 30$ m/s, FWHM = 20 nm, $b = 0$.

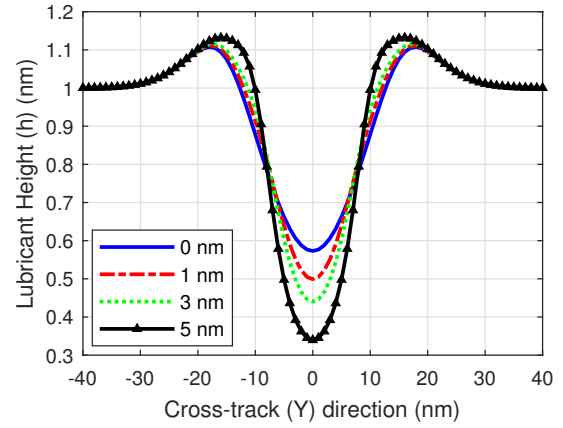
neo-hookean solution). These differences are expected to be even smaller after including disjoining pressure in both models. We thereby argue that the modified lubrication Eq. (11) is a reasonable approximation to predict lubricant deformation during HAMR.

3.3.4 Effect of Slip

In this section, we investigate the effect of slip length b on the lubricant behavior. The viscous and the slip volume flow rate (per unit width) terms in the governing Eq. (11) can be coupled together as: $q_{x,net-viscous} = \left(-\frac{h^3}{\eta} \frac{\partial p}{\partial x} \left(\frac{1}{3} + \frac{b}{h} \right) + \frac{h^2}{\eta} \tau_{b,x} \left(\frac{1}{2} + \frac{b}{h} \right) \right)$. We observe that b increases the magnitude of the viscous terms and does not (explicitly) affect the magnitude of the elastic terms. This is because the slip boundary condition (9) assumes that the slip velocity depends linearly on the wall shear stress $\tau_{xz}|_{z=0}$, $\tau_{yz}|_{z=0}$ (and not on the shear stress rate $\frac{\partial \tau_{xz}}{\partial t}|_{z=0}$, $\frac{\partial \tau_{yz}}{\partial t}|_{z=0}$). A memory slip boundary condition in which slip velocity depends on the history of the wall shear stress would affect both the viscous and elastic terms [38]. We plot the lubricant thickness after 10 ns of laser irradiation for four values of slip length: 0, 1, 3, 5 nm in Figs. 7a & 7b. As b is increased, we observe larger deformations, in particular, a larger viscous trail in the down-track profile, as expected. The cross-track profile depth also increases (i.e. larger deformation) on increase in b , but the profile width reduces. The reduction in cross-track profile width is another indicator of a change from elastic to viscous behavior (Refer Fig. 3b), on increase in slip length.



(a) Down-track lubricant profile (at $y = 0$)



(b) Cross-track lubricant profile (at $x = 100$ nm)

Fig. 7: Lubricant profile (Ztetraol) after 10 ns of laser heating. Slip Length b is varied from 0 to 5 nm. $T_{max} = 500$ °C, $U = 10$ m/s, FWHM = 20 nm.

3.3.5 Effect of Shear Modulus

In this section, we keep the thin-film viscosity $\eta_{eff}(T)$ fixed ($\eta_{eff} = 13 \times \eta_{bulk}$) and vary the shear modulus G_{eff} from 0.5 MPa to 0.1 MPa. A shear modulus of 0.5 MPa assumes that the maxwell relaxation time of the thin film lubricant is the same as the bulk lubricant (i.e. $\eta_{eff} = 13 \times \eta_{bulk}$, $G_{eff} = 13 \times G_{bulk}$, $\lambda_{eff} = \lambda_{bulk}$). As G_{eff} is decreased, the enhancement factor of 13 is partially absorbed by the Maxwell relaxation time and partially by the shear modulus. In particular, for $G_{eff} = 0.1$ MPa, $G_{eff} = 2.8 \times G_{bulk}$ and $\lambda_{eff} = 4.6 \times \lambda_{bulk}$. As the shear modulus is decreased and the maxwell relaxation time is increased, the elastic deformation increases significantly (Fig. 8).

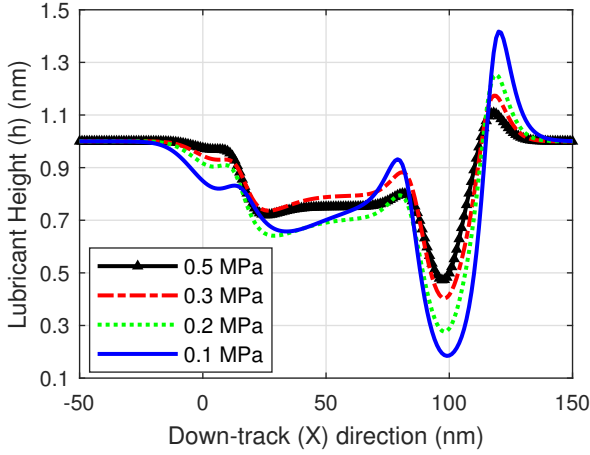


Fig. 8: Down-track lube (Ztetraol) profile (at $y = 0$) after 10 ns of laser heating. Shear Modulus G_{eff} is varied from 0.1 to 0.5 MPa with $\eta_{eff}(T)$ kept fixed. $T_{max} = 500$ °C, $U = 10$ m/s, FWHM = 20 nm, $b = 1$ nm.

3.3.6 Effect of Disk Velocity

Here we study the effect of varying the laser speed (i.e. disk velocity) on the lubricant profile, a consequence of varying the disk rotational speed. All other parameters such as disk temperature (i.e. laser power), laser FWHM and slip length were kept fixed. As the laser speed increases, the Deborah number increases ($De = \frac{\lambda U}{L}$) and hence the lubricant is expected to behave more elastically and less viscously. Fig. 9 shows plots of the lubricant profiles for four laser speeds: $U = 5$ m/s, 10 m/s, 20 m/s, 40 m/s after $\frac{150}{U}$ ns (U in m/s) of laser heating. As U is increased, the depth of the viscous trail behind the elastic trough decreases. At lower disk speeds, the lubricant has more time to respond to the laser excitation and hence leaves a larger viscous trail behind the moving laser spot.

4 Effect of Viscoelasticity on Lubricant Transfer from Media to Head during HAMR

During HAMR writing, the media is locally heated to its Curie Temperature ($T_{max,d} \sim 500$ °C), causing the disk lubricant (thickness h_d) to deform and evaporate. Evaporation increases the partial pressure of the lubricant vapor in the air bearing, p_v . Some of this vapor condenses on the relatively cooler slider surface ($T_{max,s} \sim 300$ °C), depositing a film of thickness h_s . Thus, we have three unknown profiles - $h_d(x, y, t)$, $h_s(x, y, t)$ and $p_v(x, y, t)$. A schematic of this media-to-head lubricant transfer is shown in Fig. 10. We consider two frames of reference: frame 1, which is attached to the disk and frame 2,

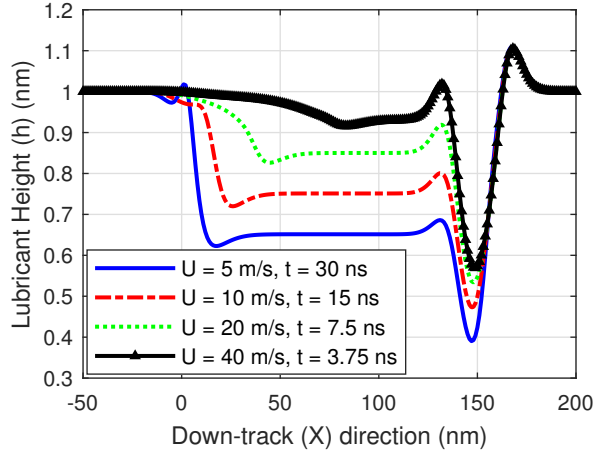


Fig. 9: Down-track lube (Ztetraol) profile (at $y = 0$) after $\frac{150}{U}$ ns of laser heating, U is varied from 5 to 40 m/s. $T_{max} = 500$ °C, FWHM = 20 nm, $b = 1$ nm.

which is attached to the slider. In frame 1, the disk is stationary and the head (and the laser spot) move with speed U along the down-track (x) direction (Fig. 10). In frame 2, the head is stationary and the disk moves (backwards) with speed U . In this study, we investigate lubricant transfer of two PFPEs - Zdol ($M_w = 1.5, 2, 2.5$ kg/mol) and Ztetraol ($M_w = 2.7$ kg/mol).

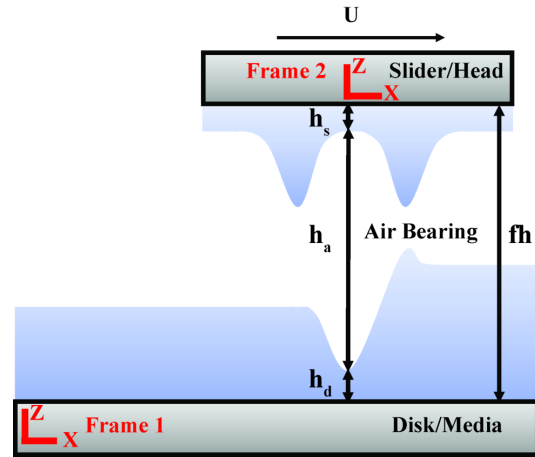


Fig. 10: HAMR lubricant transfer schematic (as seen from frame 1, which is attached to the disk): Disk lubricant of thickness h_d is subjected to a scanning laser spot of speed U . The disk lubricant evaporates to form vapor having partial pressure p_v in the HDI. The vapor condenses on the slider to form a film of thickness h_s .

4.1 Governing Equation for Disk Lubricant

The governing equation for the disk lubricant profile $h_d(x, y, t)$ is given by Eq. (11), along with Eqs. (12), (13) in frame 1 (h replaced by h_d). The net evaporation rate \dot{m}_d from the disk in Eq. (11) is determined using the Hertz-Knudsen-Langmuir law:

$$\dot{m}_d = \sqrt{\frac{M_w}{2\pi RT_d}} (p_{vap,thin} - p_v) \quad (18)$$

Here M_w is the lubricant molecular weight, R is the molar universal gas constant, T_d is the disk lubricant temperature, $p_{vap,thin}$ is the equilibrium vapor pressure of the thin-film lubricant, p_v is the partial pressure of the lubricant vapor in the air bearing. $p_{vap,thin}$ is given by the following equation: [3]

$$p_{vap,thin} = p_{vap,\infty} \exp\left(-\frac{M_w}{\rho RT_d} \pi(h_d)\right) \quad (19)$$

Here $p_{vap,\infty}$ is the bulk vapor pressure of the lubricant. The equation for p_v will be discussed in section 4.2.

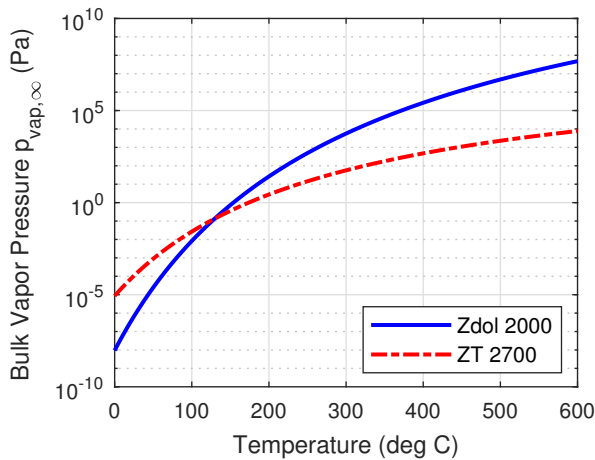


Fig. 11: Bulk equilibrium vapor pressure $p_{vap,\infty}$ versus temperature for Zdol 2000 [8] and Ztetraol 2700 [39, 40].

Karis gives the bulk vapor pressure $p_{vap,\infty}$ of Zdol as a function of temperature and molecular weight using the Clausius-Clapeyron equation [8]. This evaporation model for Zdol has also been used in previous numerical studies [3, 24]. The temperature dependent $p_{vap,\infty}$ for Ztetraol 2700 is obtained with parameters extracted using the Clausius-Clapeyron equation and the measured data in ref [39], which yields a heat of vaporization of 68.112 kJ/mol and a pre-exponential term of 685,415 Torr. This model was used by Jones et al. [40] to predict lubricant depletion in Ztetraol 2700 and was found to

agree well with experimental data. $p_{vap,\infty}$ for Zdol and Ztetraol is plotted versus temperature in Fig. 11.

4.2 Governing Equation for Lubricant Vapor

Consistent with the lubrication approximation, we assume that the density of the lubricant vapor in the air bearing, ρ_v is independent of z , i.e., $\rho_v \equiv \rho_v(x, y, t)$. The governing equation for the lubricant vapor can be obtained by integrating the continuity equation along z and applying Fick's Law of Diffusion [24, 41].

$$\begin{aligned} \frac{\partial}{\partial t}(\rho_v h_a) + \frac{\partial}{\partial x}(\rho_v q_x) + \frac{\partial}{\partial y}(\rho_v q_y) = \\ \frac{\partial}{\partial x} \left(D h_a \frac{\partial \rho_v}{\partial x} \right) + \frac{\partial}{\partial y} \left(D h_a \frac{\partial \rho_v}{\partial y} \right) + \dot{m}_d + \dot{m}_s \end{aligned} \quad (20)$$

Here $h_a \equiv (fh - h_s - h_d)$ is the air bearing height where fh is the constant head-disk spacing at the NFT (Refer Fig. 10). $q_x \equiv \int_{h_d}^{h_d+h_a} v_{a,x} dz$ and $q_y \equiv \int_{h_d}^{h_d+h_a} v_{a,y} dz$ are the volume flow rates per unit length in the x and y directions, obtained by integrating the air bearing velocity $v_{a,x}$ and $v_{a,y}$ (in frame 1) along z across the air bearing clearance. D is the lubricant vapor diffusivity in air and \dot{m}_d , \dot{m}_s are the net evaporation mass fluxes from the disk and slider lubricant films respectively.

We assume that the effects of the lubricant vapor on the air bearing pressure, temperature and velocity can be neglected. Also, the lubricant as well as air bearing temperature is simply assumed to be equal to the average of the disk and slider temperatures: $T_v \equiv \frac{T_s + T_d}{2}$. Finally, the lubricant vapor density ρ_v and partial pressure P_v are assumed to be related by the ideal gas law:

$$P_v = \frac{\rho_v R T_v}{M_w} \quad (21)$$

Our previous study [24] showed that convection has a small impact on the lubricant transfer process, however, the effect of diffusion is significant. Hence, we ignore the convective terms in Eq. (20). Diffusion coefficient D is obtained using the Hirschfelder approximation [8].

4.3 Governing Equation for the Slider Lubricant

We solve for the evolution of the lubricant film on the slider in frame 2. In this frame, the slider is stationary and the disk is moving with speed U . The temperature profile of the slider lubricant is a (stationary) Gaussian curve with FWHM of 20 nm and peak temperature $T_{max,s} = 300^\circ C$. In this frame, the governing equation

for the slider lube thickness $h_s(x, y, t)$ is again given by Eq. (11), along with Eqs. (12), (13) (h replaced by h_s). Since the temperature profile on the slider does not change with time, the thermo-capillary stress is also independent of time (Eq. (12)), $\frac{\partial \tau_{b,x}}{\partial t} = 0$, $\frac{\partial \tau_{b,y}}{\partial t} = 0$ and thus the lubricant has a predominantly viscous behavior (apart from the initial 2 ns ramp in temperature).

4.4 Results

4.4.1 Evaporation versus Thermo-capillary Stress

Using viscous simulations for Zdol at 350 °C, Dahl & Bogy [3] found that thermo-capillary stress dominates for small spot sizes (< 50 nm), whereas evaporation dominates for large spot sizes ($\sim 1 \mu\text{m}$). Here we investigate the relative importance of thermo-capillary stress vs evaporation for the viscoelastic lubricants Zdol, Ztetraol at different temperatures and spot sizes.

Figs. 12a & 12b plot the disk lubricant profile for Zdol with and without evaporation for laser FWHM of 20 nm and 1 μm and peak disk temperatures of 350 and 500 °C. For peak temperature of 350 °C, the profiles with and without evaporation are close (Cases c1 and c2) and thus thermo-capillary stress dominates for spot size of 20 nm, as reported in [3]. However, at higher temperature of 500 °C (Cases a1 and a2), evaporation dominates (even for small spot size of 20 nm). For larger spot size of 1 μm (Cases b1 and b2), evaporation becomes even more dominant. Another interesting observation is that as the spot size is increased from 20 nm to 1 μm , the Deborah number decreases ($De = \frac{\lambda U}{L}$) and hence the lubricant behavior changes from viscoelastic (Case a1: elastic trough + viscous trail) to purely viscous (Case b1: only viscous trail). We thus conclude that evaporation is the dominant mechanism for Zdol at high temperatures (~ 500 °C) for all spot sizes (20 nm to 1 μm).

Fig. 13 plots the deformation of the disk lubricant for Ztetraol with and without evaporation for laser FWHM of 20 nm (Fig. 13a) and 1 μm (Fig. 13b) and a maximum disk temperature of 500 °C. For the smaller spot size of 20 nm, the profiles with and without evaporation are almost indistinguishable (Cases a1 and a2) and thus thermo-capillary stress dominates, even at the high temperature of 500 °C (unlike Zdol). However, for larger spot size of 1 μm (Cases b1 and b2), evaporation dominates. Additionally, as the spot size is increased from 20 nm to 1 μm , the Deborah number decreases ($De = \frac{\lambda U}{L}$) and hence the lubricant behavior changes from viscoelastic (Case a1: elastic trough + viscous trail) to purely viscous (Case b1: only viscous trail).

The disparity between the dominant mechanism for Zdol vs Ztetraol at 500 °C and 20 nm (evaporation

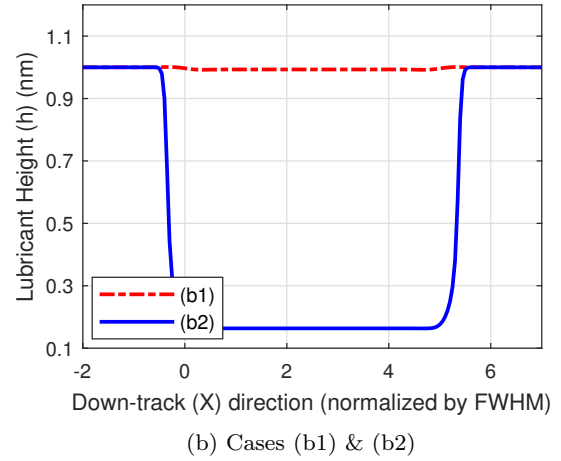
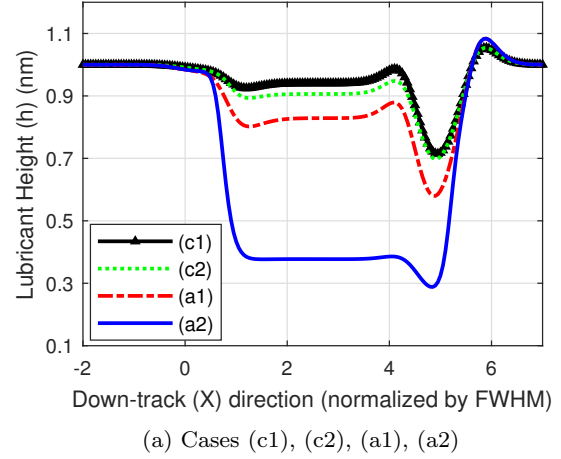


Fig. 12: Down-track disk lubricant profile with and without evaporation for Zdol 2000 after 10 ns of laser heating with $T_{max,d} = 350$ °C, 500 °C and Laser FWHM = 20 nm, 1 μm . $U = 10$ m/s, $b = 1$ nm. Case description:

- (c1) Without Evaporation, 350 °C, 20 nm, 10 ns
- (c2) With Evaporation, 350 °C, 20 nm, 10 ns
- (a1) Without Evaporation, 500 °C, 20 nm, 10 ns
- (a2) With Evaporation, 500 °C, 20 nm, 10 ns
- (b1) Without Evaporation, 500 °C, 1 μm , 0.5 μs
- (b2) With Evaporation, 500 °C, 1 μm , 0.5 μs

and thermo-capillary stress respectively) is due to the difference in vaporization properties of both lubricants. The bulk vapor pressure of Zdol at 500 °C is 4.9 MPa, while the same value for Ztetraol is only 2.3 kPa (Fig. 11). This 3 orders of magnitude difference in the vapor pressure causes the evaporation rate in Zdol to be much larger than that for Ztetraol.

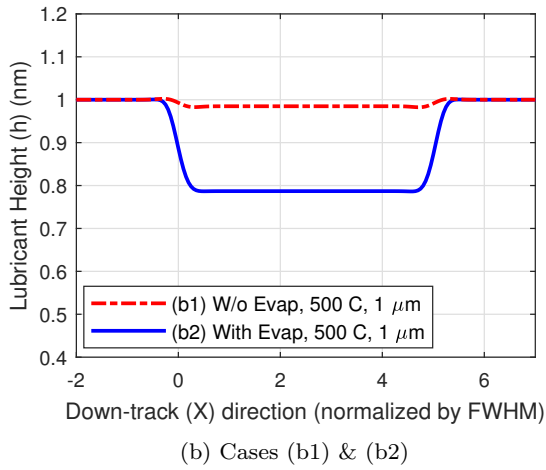
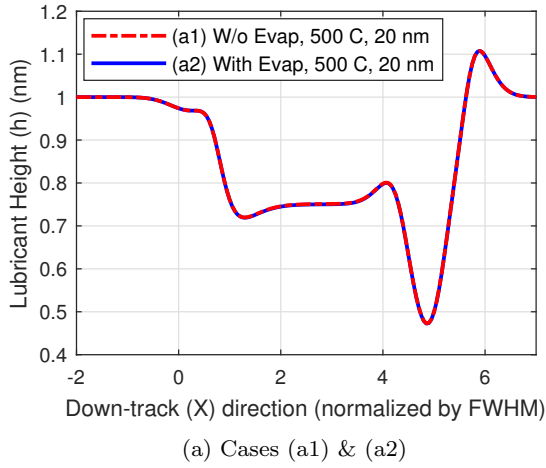


Fig. 13: Down-track disk lubricant profile with and without evaporation for Ztetraol 2700 with $T_{max,d} = 500\text{ }^{\circ}\text{C}$ and Laser FWHM = 20 nm and $1\text{ }\mu\text{m}$ respectively. $U = 10\text{ m/s}$, $b = 1\text{ nm}$. Case description:

- (a1) Without Evaporation, 500 $^{\circ}\text{C}$, 20 nm, 10 ns
- (a2) With Evaporation, 500 $^{\circ}\text{C}$, 20 nm, 10 ns
- (b1) Without Evaporation, 500 $^{\circ}\text{C}$, $1\text{ }\mu\text{m}$, $0.5\text{ }\mu\text{s}$
- (b2) With Evaporation, 500 $^{\circ}\text{C}$, $1\text{ }\mu\text{m}$, $0.5\text{ }\mu\text{s}$

4.4.2 Comparison between Zdol and Ztetraol Transfer

We assume an initially uniform film of Zdol 2000/Ztetraol 2700 of thickness $h_{0,d} = 1\text{ nm}$ on the disk. To avoid singularities, we set the initial lube thickness on the slider ($h_{0,s}$) to 0.3 nm. The slip length b is 1 nm. The disk lubricant is subjected to a moving laser spot of FWHM 20 nm at $U = 10\text{ m/s}$. The NFT center/laser spot center is located at $y = 0$ and $x = Ut$ at time t in frame 1. The resultant temperature profile on the disk and slider is a Gaussian with a peak of 500 $^{\circ}\text{C}$ and 300 $^{\circ}\text{C}$ respectively. To keep the time derivatives finite, we

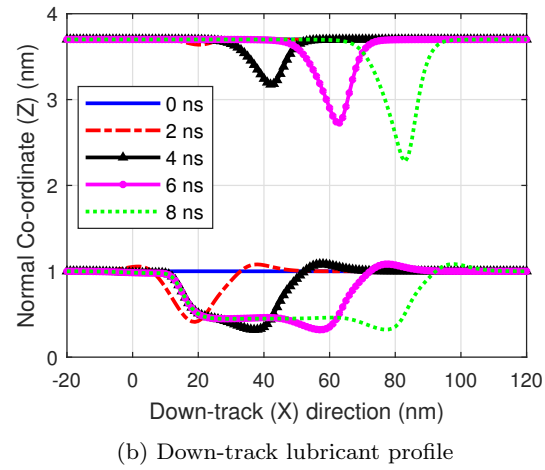
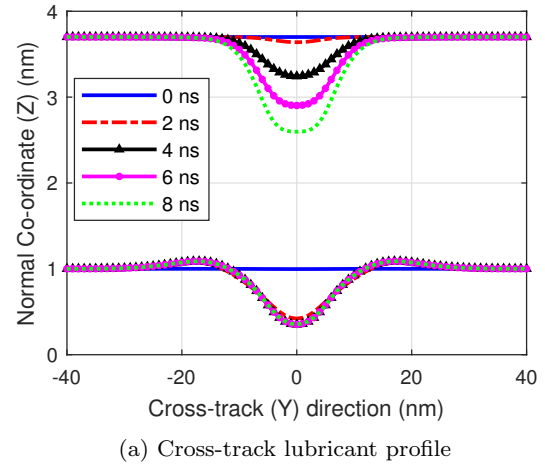


Fig. 14: Disk and slider lubricant profiles at different times of laser irradiation in cross-track and down-track directions for Zdol 2000. $T_{max,d} = 500\text{ }^{\circ}\text{C}$, $T_{max,s} = 300\text{ }^{\circ}\text{C}$, $U = 10\text{ m/s}$, FWHM = 20 nm, $b = 1\text{ nm}$.

apply the initial rise in temperature on the disk/slider as a ramp of 2 ns. The head-disk clearance fh is 4 nm.

Figs. 14a & 14b show the time evolution of the lubricant profiles on the disk (bottom curves) and the slider (top curves) in the cross-track and down-track directions for Zdol 2000, as viewed from frame 1. The down-track profile is plotted at $y = 0$, the cross-track profile is plotted at $x = Ut$ (i.e. at instantaneous location of laser spot/NFT). In frame 1, the disk is stationary and the slider is moving, hence the slider lubricant profile moves forward in the down-track direction as time proceeds. On the disk, the length of the depleted region increases as the scanning laser moves forward in the down-track direction. As disk lubricant depletion increases with time, lubricant accumulation on the head grows. The simulation predicts a peak lube height of 1.7 nm on the slider after 8 ns.

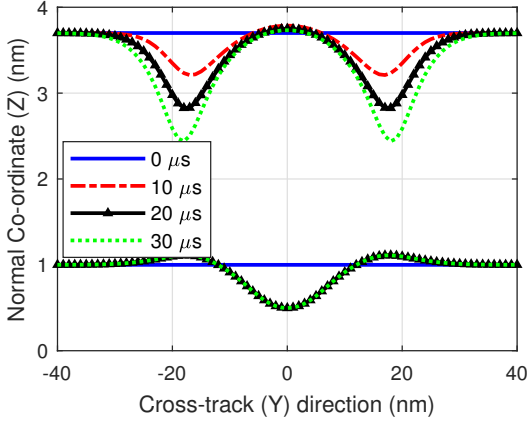
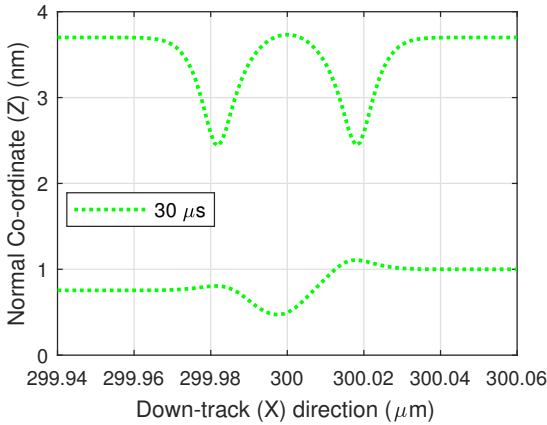
(a) Cross-track lubricant profile at $t = 0, 10, 20, 30 \mu\text{s}$ (b) Down-track lubricant profile at $t = 30 \mu\text{s}$

Fig. 15: Disk and slider lubricant profiles at different times of laser irradiation in cross-track and down-track directions for Ztetraol 2700. $T_{max,d} = 500 \text{ }^\circ\text{C}$, $T_{max,s} = 300 \text{ }^\circ\text{C}$, $U = 10 \text{ m/s}$, $\text{FWHM} = 20 \text{ nm}$, $b = 1 \text{ nm}$.

Figs. 15a & 15b show the time evolution of lubricant profiles on the disk (bottom curves) and the slider (top curves) in the cross-track and down-track directions for Ztetraol, as viewed from frame 1. We observe a significant difference between the rates of lubricant transfer for Zdol vs Ztetraol. While lubricant transfer occurs on a time scale of ns for Zdol, lubricant pick-up occurs on a time scale of μs for Ztetraol. This can be attributed to the difference in vaporization properties of both lubricants - bulk vapor pressure of Zdol at $500 \text{ }^\circ\text{C}$ is 4.9 MPa , while that for Ztetraol is only 2.3 kPa (Fig. 11).

The shape of the slider lubricant profile is also different for the two lubricants. For Zdol, the slider lubricant height is maximum at the NFT center and the lubricant height decreases radially away from the NFT (Fig. 14a & 14b). On the other hand, for Ztetraol, we see a minima in the slider lubricant height at the NFT center (Figs. 15a

& 15b). Radially away from the NFT, the head lubricant thickness initially increases, achieves a maximum at a radial position of $\sim 18 \text{ nm}$ and thereafter decreases. This difference can be explained by the relative dominance of evaporation/condensation vs thermo-capillary stress. For Zdol, disk lubricant evaporation rate is so high that condensation of lubricant onto the slider dominates over thermo-capillary stress. Since the disk temperature is maximum at the NFT center, the evaporation rate and slider lubricant height are also maximized here. On the other hand, with much slower evaporation rate for Ztetraol, thermo-capillary stress dominates and hence a minima of slider lubricant height is observed at the NFT center (where the slider temperature is maximum). The condensed lubricant is pushed away from the NFT center by the thermo-capillary stress, causing the observed lump of accumulated lubricant at a radial position of $\sim 18 \text{ nm}$ from the NFT center.

4.4.3 Effect of Lubricant Molecular Weight

In order to investigate the effect of lubricant molecular weight on the transfer dynamics, we performed simulations for Zdol with 3 different molecular weights - 1.5, 2 and 2.5 kg/mol . All other properties of the lubricants (viscosity, shear modulus, disjoining pressure) are assumed to be the same. As the molecular weight is increased, the equilibrium vapor pressure as well as evaporation rate decreases (lighter molecules evaporate faster) [8]. Hence, the amount of lubricant transfer for the low molecular weight lubricant is larger than that for the high molecular weight lubricant (Fig. 16).

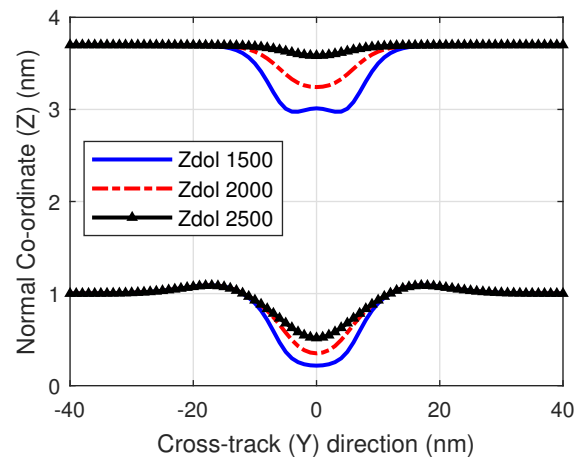


Fig. 16: Disk and slider lubricant profiles in cross-track direction after 4 ns of laser irradiation for Zdol 1500, 2000 and 2500. $T_{max,d} = 500 \text{ }^\circ\text{C}$, $T_{max,s} = 300 \text{ }^\circ\text{C}$, $U = 10 \text{ m/s}$, $\text{FWHM} = 20 \text{ nm}$, $b = 1 \text{ nm}$.

4.4.4 Viscous vs Viscoelastic Solution

In this section, we compare the viscoelastic solution with the purely viscous case (elastic terms artificially suppressed: $q_{elastic} = 0$ in Eq. (11)). We plot the cross-track lubricant profile (Ztetraol) on disk and head at the end of 10 μs of laser irradiation for the viscoelastic and purely viscous cases in Fig. 17. The slip length b is set to 1 nm. All other parameters are same as Section 4.4.2. Similar to Fig. 3b, the deformed lubricant width on the disk for the viscoelastic solution is much larger (almost twice) the width of the purely viscous solution. The depth of the deformed viscoelastic solution on the disk is also larger than the viscous solution. Disjoining pressure suppresses the equilibrium vapor

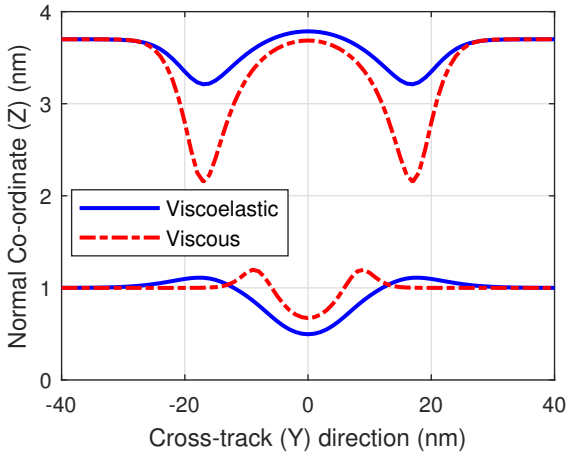


Fig. 17: Disk and slider lubricant profiles in cross-track direction after 10 μs of laser irradiation for Ztetraol - viscoelastic vs viscous solution. $T_{max,d} = 500$ °C, $T_{max,s} = 300$ °C, $U = 10$ m/s, FWHM = 20 nm, $b = 1$ nm.

pressure of the thin film lubricant (Eq. (19)). If the lubricant thickness h_d is smaller, its disjoining pressure is larger (Eq. (13)) and hence its thin-film equilibrium vapor pressure and evaporation rate are smaller. The disk lubricant thickness of the viscoelastic solution is smaller than the viscous solution (near the laser spot center), causing the evaporation rate from the disk to be smaller, compared to the viscous solution. Hence, the amount of condensed lubricant on the head is also smaller for the viscoelastic solution.

4.4.5 Effect of Slip

Next, we investigate the impact of slip on the lubricant transfer process. We plot the cross-track lubricant profile on disk and slider after 10 μs of laser heating for

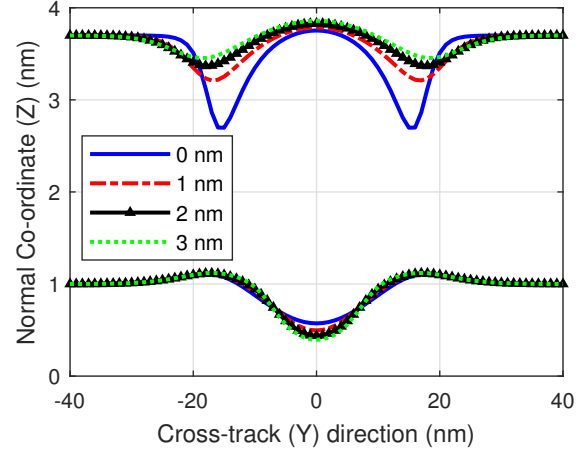


Fig. 18: Disk and slider lubricant profiles in cross-track direction after 10 μs of laser irradiation for Ztetraol. Slip Length (b) varied from 0 to 3 nm. $T_{max,d} = 500$ °C, $T_{max,s} = 300$ °C, $U = 10$ m/s, FWHM = 20 nm.

Ztetraol in Fig. 18. The slip length b is varied: 0, 1, 2 and 3 nm. All other parameters are kept fixed (same as Section 4.4.2). As b is increased, the disk lubricant profile depth increases (i.e. larger viscous deformations, similar to Fig. 7b). The resultant smaller disk lubricant thickness near the laser spot center causes the evaporation rate from the disk to be smaller for larger b (due to larger disjoining pressure for thinner film), decreasing the amount of lubricant transfer. Accordingly, the slider lubricant height decreases as the slip length is increased.

4.4.6 Disjoining Pressure Study

Due to the close relation between disjoining pressure and evaporation rate, we study the effect of disjoining pressure on lubricant transfer. We consider three models - DP1: $A_{VLS} = 1e-19$ J, DP2: $A_{VLS} = 3e-20$ J, DP3: temperature dependent A_{VLS} from [4]. The same physics of molecular interactions and their changes with temperature applies to surface tension and interfacial energetics. Marchon & Saito [4] have proposed a temperature dependent Hamaker constant defined as:

$$\begin{aligned} A_{VLS} &= \sqrt{A_{LL}A_{SS}} - A_{LL} \\ A_{LL} &= A_{LL}^0(1 - s\Delta T) \end{aligned} \quad (22)$$

Here A_{SS} and A_{LL} are Hamaker constants for solid-solid interactions and liquid-liquid interactions respectively. A_{LL} is assumed to have a linear dependence on temperature, similar to surface tension. We use the same values as those proposed by Marchon: $A_{LL}^0 = 3.78e-20$ J, $s = 1.72e-3$ °C⁻¹, $A_{SS} = 1.16e-19$ J. The resulting

$A_{VLS}(T)$ varies from $\sim 3e-20$ J at 0°C to 0 at $\sim 600^\circ\text{C}$ [4]. The magnitude of disjoining pressure decreases in the order $DP1 > DP2 > DP3$. Fig. 19 shows that the amount of lubricant accumulated on the head increases as the disjoining pressure decreases from DP1 to DP3.

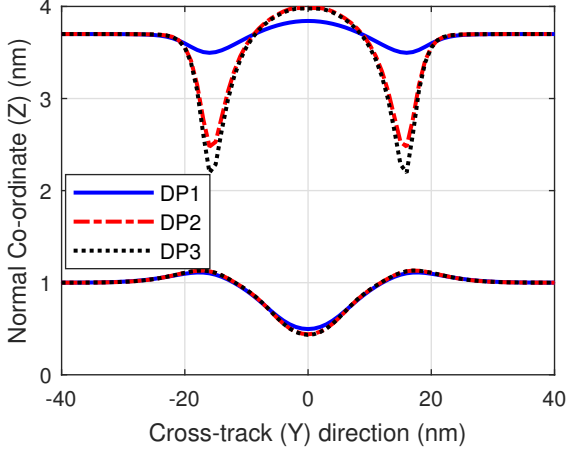
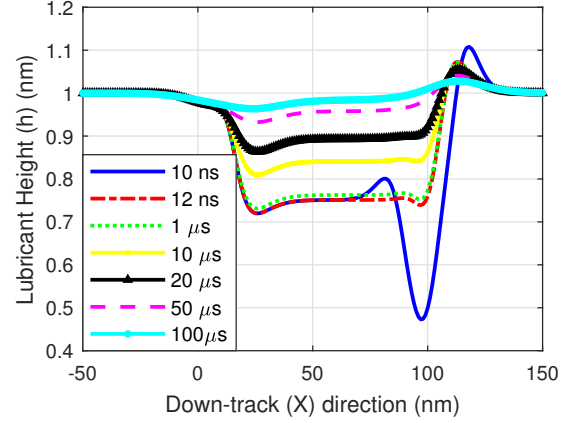


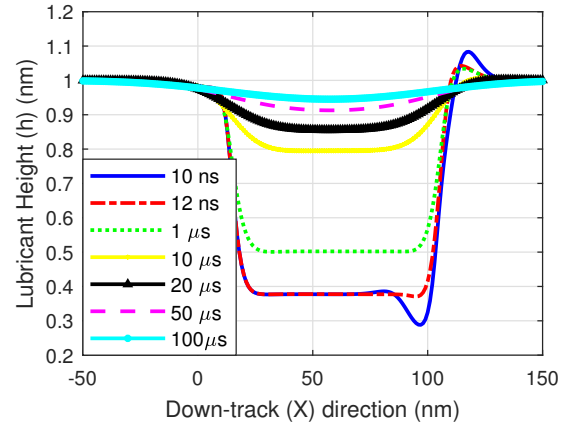
Fig. 19: Disk and slider lubricant profiles in cross-track direction after $3 \mu\text{s}$ of laser irradiation for Ztetraol for different disjoining pressure models - DP1: $A_{VLS} = 1e-19$ J, DP2: $A_{VLS} = 3e-20$ J, DP3: temperature dependent A_{VLS} from [4]. $T_{max,d} = 500^\circ\text{C}$, $T_{max,s} = 300^\circ\text{C}$, $U = 10$ m/s, FWHM = 20 nm, $b = 1$ nm.

5 Lubricant Recovery after Writing

We next study the recovery of the lubricant after the laser is turned off. The lubricant is subjected to a moving laser spot at 10 m/s for 10 ns. The laser is then turned off and the temperature drop is modeled as a 2 ns ramp ($T_{max} = 500^\circ\text{C}$ at $t = 10$ ns and $T_{max} = 25^\circ\text{C}$ at $t = 12$ ns). The slip length b is 1 nm. The blue curve in Fig. 20a is the down-track lubricant profile for Ztetraol after 10 ns of laser heating. We see a viscous trail and an elastic trough. As the disk temperature falls to ambient at $t = 12$ ns, the elastic trough recovers instantaneously (time scale of ns) leaving behind only the viscous trail (Red curve in Fig. 20a). Thereafter, the viscous trail recovers slowly under the influence of disjoining pressure over a time scale of μs , as predicted in viscous simulations [5]. A similar trend - instantaneous recovery of elastic trough from 10 ns to 12 ns, followed by slow recovery of viscous/evaporation trail is observed for Zdol in Fig. 20b. In order to compare the recovery of Zdol and Ztetraol, we plot the minimum lubricant height versus time for both lubricants in Fig. 21. The



(a) Ztetraol 2700 Recovery



(b) Zdol 2000 Recovery

Fig. 20: Lubricant recovery after 10 ns of writing. $T_{max} = 500^\circ\text{C}$, $U = 10$ m/s, FWHM = 20 nm, $b = 1$ nm.

viscosity of Ztetraol at 25°C is ~ 7 times that of Zdol [8]. Hence, the recovery rate (slope of Fig. 21) of Zdol during the second stage (recovery of the viscous/evaporation trail) is larger than that of Ztetraol.

6 Discussion

Our simulations indicate that PFPE lubricants exhibit a combination of viscous and elastic behavior at the timescale of HAMR. When subjected to a scanning laser spot of 20 nm FWHM at 10 m/s, the disk lubricant profile consists of an elastic trough centered at the instantaneous laser location, followed by a viscous trail (Fig. 2). The viscous vs elastic behavior of the lubricant is a function of the Deborah number, $De = \frac{\lambda U}{L}$. At a laser spot size (L) of $1 \mu\text{m}$ (low De), the lubricant exhibits purely viscous behavior (Fig. 13b). However, as L is reduced to 20 nm, the Deborah number decreases, causing the lubricant to behave part-viscous, part-elastic

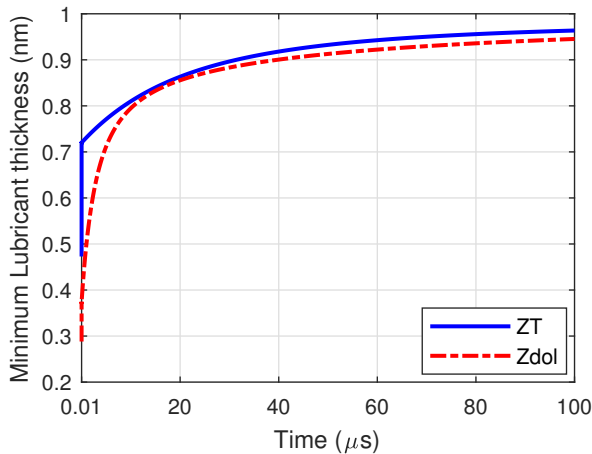


Fig. 21: Lubricant recovery: Zdol 2000 vs Ztetraol 2700.

(Figs. 3a, 13a). A similar change in behavior (viscous to elastic) is observed as the laser velocity (U) is increased from 5 m/s to 40 m/s (Fig. 9).

In order to estimate the magnitude of non-linear viscoelastic effects, we compared the lubricant deformation using the non-linear elastic neo-hookean model with our Linear Maxwell model, in the limit $De \rightarrow \infty$ (Fig. 6). Our results suggest that the non-linear effects are relatively small in the elastic limit; nevertheless, the model presented here can be improved by using a non-linear viscoelastic constitutive equation. We also compare the results of our modified lubrication equation with the 3D ANSYS model proposed by Sarabi & Bogoy [10]. We find a good agreement between both models, validating the lubrication approximation (Fig. 5).

The high thermo-capillary stress on the lubricant during HAMR would likely be effective at debonding the functional groups from the disk, thereby promoting slippage of lubricant molecules [11]. Due to the lack of experimental data for the value of slip lengths at the HDI, we conduct a parametric study of the effect of slip on lubricant deformation. As the slip length is increased, the lubricant flow rate increases, causing larger deformations (Figs. 7a & 7b). With the Navier slip boundary condition (linear dependence of slip velocity on shear stress), slip increases the net viscous flow rate, causing a change in behavior from elastic to viscous.

The relative importance of thermo-capillary stress vs evaporation for lubricant deformation during HAMR depends on its vaporization properties, laser spot size and peak temperature. Thermo-capillary stress is proportional to the spatial temperature gradient and increases as the spot size is decreased or the peak temperature is increased. Evaporation rate also increases on increase in peak temperature. At low temperatures (~ 350 °C),

thermo-capillary stress dominates at small spot sizes (~ 20 nm) and evaporation dominates at large spot sizes (~ 1 μm) for Zdol [3]. However, at high temperatures (~ 500 °C), evaporation dominates at all spot sizes - 20 nm to 1 μm (Figs. 12a & 12b). On the other hand, for Ztetraol, thermo-capillary shear stress dominates over evaporation for smaller spot sizes (~ 20 nm), even at high temperatures ~ 500 °C (Fig. 13a). However, evaporation dominates for larger spot sizes (~ 1 μm in Fig. 13b). The disparity between the dominant mechanism for Zdol vs Ztetraol at 500 °C, 20 nm (evaporation and thermo-capillary stress respectively) is due to the difference in their vaporization properties (Fig. 11). This also leads to a significant difference in the rates of media-to-head lubricant transfer for Zdol (timescale of ns - Fig. 14a) vs Ztetraol (timescale of μs - Fig. 15a).

The media-to-head lubricant transfer causes a deposition of media contaminants at the NFT. A quantitative understanding of this material transfer is necessary to mitigate its effect. In our previous publication [24], we studied the effect of media/head temperature and initial lubricant thickness on lubricant transfer, with a viscous model for Zdol. We found that the amount of transfer increases on increase in media temperature and initial lubricant thickness. Comparatively, the head temperature has a small impact on the transfer dynamics. In this study, we have improved the previous model to investigate the effect of viscoelasticity, slippage and disjoining pressure on lubricant pick-up.

The predicted disk lubricant deformation using a purely viscous model is smaller than the deformation due to a viscoelastic constitutive equation (Fig. 17). This difference causes the viscous model to over-predict the amount of transfer, compared to the viscoelastic model. Including viscoelastic effects is thus essential to accurately estimate the rate of lubricant transfer.

Disjoining pressure suppresses the evaporation rate of the thin-film lubricant (Eqs. (18), (19)). Hence, the amount of lubricant transfer increases as the Hamaker constant is decreased (Fig. 19). Slip increases the flow rate of the disk lubricant, causing larger deformations. Accordingly, as the slip length is increased, the disk lubricant thickness near the laser spot center decreases, restricting the amount of transfer (due to larger disjoining pressure for the thinner film, Fig. 18).

The recovery of the viscoelastic lubricant post-writing has two time scales. When the laser is turned off, the elastic trough recovers instantaneously (\sim ns), leaving behind the viscous/evaporation trail (Fig. 20a & 20b). Thereafter, the trail recovers over a time scale of μs . The recovery of the viscous/evaporation trail depends on the lubricant disjoining pressure, viscosity and the initial deformed profile [5]. The viscous recovery rate

for Zdol is faster than that for Ztetraol, primarily due to the higher viscosity of Ztetraol at 25 °C. (Fig. 21)

In this study, we have not considered the effects of thermal decomposition [42] or polydispersity [43]. The reduction of effective viscosity at high shear stresses is presumed to be due to slip by Mate et al. [11]. However, at high shear strains, viscosity reduction could also occur due to shear thinning [44]. Itoh et al. have reported occurrence of shear thinning in Fiber Wobbling Experiments [27]. We have assumed that no shear thinning occurs in this study. As a first order approximation, we can assume that shear thinning decreases the viscosity and maxwell relaxation time ($\eta(\dot{\gamma})$, $\lambda(\dot{\gamma})$), while the shear modulus is unaffected ($G = \text{constant}$). With this assumption, if shear thinning does occur, we would expect to see larger, viscous deformations in the lubricant response. At low fly heights, environmental conditions such as humidity also influence the interactions in the head-disk interface. Kim et. al. found that disk-to-head lubricant transfer is proportional to AH, absolute amount of water in the system, rather than RH, Relative Humidity of the system alone [45]. The effect of humidity is not considered in this study. Finally, we have only considered thermal transfer mechanisms in this study. At low fly heights, the disk lubricant disjoining pressure is influenced by the presence of the slider and the lubricant layer on the slider [24]. This would result in increased lubricant pick-up due to dewetting [46].

7 Conclusion

We have introduced a modification to the traditional Reynolds lubrication equation using the Linear Maxwell constitutive equation and a slip boundary condition. We have used this equation to predict the deformation and recovery of the disk lubricant due to HAMR laser heating under the influence of thermo-capillary stress and disjoining pressure. When subjected to a 20 nm FWHM scanning laser spot, the lubricant profile consists of an elastic trough centered at the instantaneous laser location, followed by a viscous trail. When the laser is turned off, the elastic trough recovers instantaneously, leaving behind the viscous trail, which recovers over a time scale of μs . Slippage increases the flow rate of the lubricant, causing larger viscous deformations.

Subsequently, we used this modified lubrication equation to develop a model that predicts the media-to-head lubricant transfer during HAMR. This model simultaneously determines the deformation and evaporation of the viscoelastic lubricant film on the disk, the diffusion of the lubricant vapor in the air bearing and the evolution of the condensed lubricant film on the slider. We have investigated the effects of viscoelasticity, lubricant type

(Zdol vs Ztetraol), molecular weight, slip velocity and disjoining pressure on the lubricant transfer process. Our results show a significant difference between the rates of transfer for Zdol ($\sim \text{ns}$) vs Ztetraol ($\sim \mu\text{s}$). As the lubricant molecular weight is decreased, the evaporation rate and amount of transfer increase. The predicted disk lubricant deformation using a purely viscous model is smaller than the deformation due to a viscoelastic model, causing the viscous model to over-predict the amount of transfer. The amount of transfer decreases on increase in slip length and increase in disjoining pressure.

Acknowledgements This work was supported by the Computer Mechanics Laboratory at University of California, Berkeley, Mechanical Engineering Department. This is a post-peer-review, pre-copyedit version of an article published in Tribology Letters. The final authenticated version is available online at: <http://dx.doi.org/10.1007/s11249-018-1100-4>

References

1. Marchon, B., Guo, X.C., Pathem, B.K., Rose, F., Dai, Q., Feliss, N., Schreck, E., Reiner, J., Mosendz, O., Takano, K., Do, H., Burns, J., Saito, Y.: Head-disk interface materials issues in heat-assisted magnetic recording. IEEE Trans. Magn. (2014). <https://doi.org/10.1109/TMAG.2013.2283068>
2. Wu, L.: Modelling and simulation of the lubricant depletion process induced by laser heating in heat-assisted magnetic recording system. Nanotechnology (2007). <https://doi.org/10.1088/0957-4484/18/21/215702>
3. Dahl, J.B., Bogy, D.B.: Lubricant flow and evaporation model for heat-assisted magnetic recording including functional end-group effects and thin film viscosity. Tribol. Lett. (2013). <https://doi.org/10.1007/s11249-013-0190-2>
4. Marchon, B., Saito, Y.: Lubricant thermodiffusion in heat assisted magnetic recording. IEEE Trans. Magn. (2012). <https://doi.org/10.1109/TMAG.2012.2194138>
5. Dahl, J.B., Bogy, D.B.: Simulation of lubricant recovery after heat-assisted magnetic recording writing. Tribol. Lett. (2013). <https://doi.org/10.1007/s11249-013-0203-1>
6. Kono, R-N, Izumisawa, S., Jhon, M.S., Kim, C.A., Choi, H.J.: Rheology of perfluoropolyether lubricants. IEEE Trans. Magn. (2001). <https://doi.org/10.1109/20.950980>
7. Choi, H.J., Lim, S., Izumisawa, S., Jhon, M.S.: Viscoelasticity and solution viscosity of perfluoropolyether lubricants. Tribol. Int. (2005). <https://doi.org/10.1016/j.triboint.2005.01.024>
8. Karis, T.: Lubricants for the disk drive industry. In: Rudnick L. (eds) Lubricant Additives: Chemistry and Applications, chap 22. CRC Press, Boca Raton, FL, pp. 523584 (2009)
9. Tanner, R.I.: Engineering Rheology. Clarendon Press, Oxford (2000)
10. Sarabi, S. & Bogy, D.B.: Effect of Viscoelasticity on Lubricant Behavior Under Heat-Assisted Magnetic Recording Conditions. Tribol. Lett. (2018). <https://doi.org/10.1007/s11249-017-0979-5>
11. Mate, C.M., Marchon, B., Murthy, A., Kim, S-H.: Lubricant-Induced Spacing Increases at Slider-Disk Interfaces in Disk Drives. Tribol. Lett. (2010). <https://doi.org/10.1007/s11249-009-9555-y>

12. Kiely, J.D., Jones, P.M., Y.Yang, Brand, J.L., Anaya-Dufresne, M., Fletcher, P.C., Zavaliche, F., Toivola, Y., Duda, J.C., Johnson, M.T.: Write-induced head contamination in heat-assisted magnetic recording. *IEEE Trans. Magn.* (2017). <https://doi.org/10.1109/TMAG.2016.2618842>
13. Xiong, S., Wang, N., Smith, R., Li, D., Schreck, E., Dai, Q.: Material transfer inside head disk interface for heat assisted magnetic recording. *Tribol. Lett.* (2017). <https://doi.org/10.1007/s11249-017-0860-6>
14. Yang, Y., Li, X., Stirniman, M., Yan, X., Huang, F., Zavaliche, F., Wang, H., Huang, J., Tang, H., Jones, P.M., Kiely, J.D., Brand, J.L.: Head-disk lubricant transfer and deposition during heat-assisted magnetic recording write operations. *IEEE Trans. Magn.* (2015). <https://doi.org/10.1109/TMAG.2015.2434826>
15. Aoyama, J., Furukawa, M., Nishida, S., Tasaka, K., Matsuda, K., Kuroki, K. and Ikeda, M.: A Head Cleaning Procedure for Heat-Assisted Magnetic Recording. *IEEE Trans. Magn.* (2017). <https://doi.org/10.1109/TMAG.2017.2706981>
16. Kiely, J., Jones, P., Hoehn, J.: Materials challenges for the heat-assisted magnetic recording head-disk interface. *MRS Bulletin* (2018). <https://doi.org/10.1557/mrs.2018.4>
17. Tani, H., Uesaraie, Y., Lu, R., Koganezawa, S., Tagawa, N.: Smear growth on head slider surface from siloxane outgas on heat assisted magnetic recording. *Microsyst. Technol.* (2018). <https://doi.org/10.1007/s00542-018-3839-9>
18. Dai, X., Li, H., Shen, S. and Wu S.: Study of Perfluoropolyether Lubricant Consumption and Recovery in Heat Assisted Magnetic Recording Using Molecular Dynamics Simulation Method. *IEEE Trans. Magn.* (2017). <https://doi.org/10.1109/TMAG.2016.2637872>
19. Dai, X., Zhang, J., Shen, S., Li, H., Zhai, T., Wu, S., Liu, S. and Du, H.: Study of Formation and Development of Lubricant Bridge in Head - Disk Interface Using Molecular Dynamic Method. *IEEE Trans. Magn.* (2017). <https://doi.org/10.1109/TMAG.2016.2626459>
20. Seo, Y., Pan, D., Ovcharenko, A., Yang, M. and Talke, F.: Molecular Dynamics Simulation of Lubricant Transfer at the Head-Disk Interface. *IEEE Trans. Magn.* (2014). <https://doi.org/10.1109/TMAG.2014.2322353>
21. Seo, Y., Ovcharenko, A. and Talke, F.: Simulation of Hydrocarbon Oil Contamination at the Head-Disk Interface Using Molecular Dynamics. *Tribol. Lett.* (2016). <https://doi.org/10.1007/s11249-016-0648-0>
22. Mate, C.M. and Marchon, B.: Shear Response of Molecularly Thin Liquid Films to an Applied Air Stress. *Phys. Rev. Lett.* (2000). <https://doi.org/10.1103/PhysRevLett.85.3902>
23. Scarpulla, M., Mate, C.M., Carter, M.: Air shear driven flow of thin perfluoropolyether polymer films. *J. Chem. Phys.* (2003). <https://doi.org/10.1063/1.1536953>
24. Sakhalkar, S.V. & Bogy, D.B.: A Model for Lubricant Transfer from Media to Head During Heat-Assisted Magnetic Recording (HAMR) Writing. *Tribol. Lett.* (2017). <https://doi.org/10.1007/s11249-017-0952-3>
25. Ruths, M. and Granick, S.: Tribology of confined Fomblin-Z perfluoropolyalkylethers: molecular weight dependence and comparison between unfunctionalized and telechelic chains. *Tribol. Lett.* (1999). <https://doi.org/10.1023/A:1019137824102>
26. Itoh, S., Fukuzawa, K., Hamamoto, Y., Zhang, H., Mitsuya, Y.: Fiber Wobbling Method for Dynamic Viscoelastic Measurement of Liquid Lubricant Confined in Molecularly Narrow Gaps. *Tribol. Lett.* (2008). <https://doi.org/10.1007/s11249-008-9325-2>
27. Itoh, S., Fukuzawa, K., Hamamoto, Y., Zhang, H.: Opposing effects of confinement and confinement-induced shear-thinning on viscoelastic properties of liquid lubricant in nanometer-scale gaps. *Tribol. Int.* (2011). <https://doi.org/10.1016/j.triboint.2010.07.007>
28. Karis, T., Marchon, B., Flores, V., Scarpulla, M.: Lubricant spin-off from magnetic recording disks. *Tribol. Lett.* (2001). <https://doi.org/10.1023/A:1012553415639>
29. Marchon, B., Guo, X.C., Moser, A., Spool, A., Kroeker, R., Crimi, F.: Lubricant dynamics on a slider: The waterfall effect. *J. Appl. Phys.* (2009). <https://doi.org/10.1063/1.3104764>
30. Rajagopal, K. R. : On some unresolved issues in non-linear fluid dynamics. *Russ. Math. Surv* (2003). <https://doi.org/10.1070/RM2003v058n02ABEH000612>
31. Rauscher, M., Munch, A., Wagner, B., Blosssey, R.: A thin-film equation for viscoelastic liquids of Jeffreys type. *Eur. Phys. J. E* (2005). <https://doi.org/10.1140/epje/i2005-10016-8>
32. Blosssey, R.: Thin film rupture and polymer flow. *Phys. Chem. Chem. Phys.* (2008). <https://doi.org/10.1039/b807728m>
33. Wu, L.: Lubricant dynamics under sliding condition in disk drives. *J. Appl. Phys.* (2006). <https://doi.org/10.1063/1.2220489>
34. Mate, C.M.: Taking a fresh look at disjoining pressure of lubricants at slider-disk interfaces. *IEEE Trans. Magn.* (2011). <https://doi.org/10.1109/TMAG.2010.2073691>
35. LeVeque, R.: *Finite Difference Methods for Ordinary and Partial Differential Equations*. SIAM, Philadelphia, PA (2007). <https://doi.org/10.1137/1.9780898717839>
36. Christensen, R.: *Theory of viscoelasticity: an introduction*. Elsevier (2012).
37. Tichy, J.: Non-Newtonian Lubrication With the Convected Maxwell Model. *J. Tribol.* (1996). <https://doi.org/10.1115/1.2831307>
38. Schowalter, W: The behaviour of complex fluids at solid boundaries, *J. Non-Newtonian Fluid Mech.* (1988). [https://doi.org/10.1016/0377-0257\(88\)85048-1](https://doi.org/10.1016/0377-0257(88)85048-1)
39. Solvay-Solexis: Fomblin Z Derivatives: Product Data Sheet. Solvay Solexis, Inc., North America (2002)
40. Jones, P.M., Yan, X., Hohlfield, J., Stirniman, M., Kiely, J.D., Zavaliche, F., Tang, H.H.: Laser-induced thermodesorption of perfluoropolyether lubricant from the surface of a heat-assisted magnetic recording disk: Lubricant evaporation and diffusion. *Tribol. Lett.* (2015). <https://doi.org/10.1007/s11249-015-0561-y>
41. Wu, L.: A model for liquid transfer between two approaching gas bearing surfaces through coupled evaporation-condensation and migration dynamics. *J. Appl. Phys.* (2008). <https://doi.org/10.1063/1.2951616>
42. Lei, R.Z., Gellman, A.J., Jones, P.: Thermal Stability of Fomblin Z and Fomblin Zdol Thin Films on Amorphous Hydrogenated Carbon. *Tribol. Lett.* (2001). <https://doi.org/10.1023/A:1016670303657>
43. Zhou, W., Zeng, Y., Liu, B., Yu, S., Hua, W., Huang, X.: Evaporation of polydisperse perfluoropolyether lubricants in heat-assisted magnetic recording. *Appl. Phys. Express* (2011). <https://doi.org/10.1143/APEX.4.095201>
44. Zhang, Y., Polycarpou, A.: A single asperity sliding contact model for molecularly thin lubricant. *Microsyst. Technol.* (2017) <https://doi.org/10.1007/s00542-016-2910-7>
45. Kim, S. H., Dai, Q., Marchon, B., Flechsig, K.: Humidity effects on lubricant transfer in the head-disk interface of a hard disk drive. *J. Appl. Phys.* (2009). <https://doi.org/10.1063/1.3061704>

46. Ambekar, R.P., Bogy, D.B., Dai, Q., Marchon, B.: Critical clearance and lubricant instability at the head-disk interface of a disk drive. *Appl. Phys. Lett.* (2008). <https://doi.org/10.1063/1.2837187>